The transient start of supersonic jets

MATEI I. RADULESCU† AND CHUNG K. LAW

Mechanical and Aerospace Engineering, Princeton, NJ 08544, USA
mradules@princeton.edu

This study investigates the initial transient hydrodynamic evolution of highly under-expanded slit and round jets. A closed-form analytic similarity solution is derived for the temporal evolution of temperature, pressure and density at the jet head for vanishing diffusive fluxes, generalizing a previous model of Chekmarev using Chernyi's boundary-layer method for hypersonic flows. Two-dimensional numerical simulations were also performed to investigate the flow field during the initial stages over distances of $\sim$1000 orifice radii. The parameters used in the simulations correspond to the release of pressurized hydrogen gas into ambient air, with pressure ratios varying between approximately 100 and 1000. The simulations confirm the similarity laws derived theoretically and indicate that the head of the jet is laminar at early stages, while complex acoustic instabilities are established at the sides of the jet, involving shock interactions within the vortex rings, in good agreement with previous experimental findings. Very good agreement is found between the present model, the numerical simulations and previous experimental results obtained for both slit and round jets during the transient establishment of the jet. Criteria for Rayleigh–Taylor instability of the decelerating density gradients at the jet head are also derived, as well as the formulation of a model addressing the ignition of unsteady expanding diffusive layers formed during the sudden release of reactive gases.

1. Introduction

Highly unsteady under-expanded jets occur when a high-pressure gas suddenly discharges into a lower-pressure gas through an orifice or nozzle. The emerging high-pressure gas acts as a piston and drives a strong shock into the lower-pressure gas. The multi-dimensional expansion of the shocked gases leads to the weakening of the lead shock, but also to the formation of secondary inward-propagating shocks created due to the faster rate of expansion of the high-pressure gas escaping from the discharge orifice. An example is the well-known problem of the start-up of a hypersonic nozzle, consisting of a shock transmission through a converging–diverging nozzle (Smith 1966; Amman 1969). When the divergence angle increases to 90° as for an unconfined expansion, the outflow is no longer streamlined and the preferential momentum of the gas along the jet axis gives rise to highly complex vortex rings and interacting shocks. A series of schlieren photographs taken by Naboko *et al.* (1972) illustrating the transient jet formation process is shown in figure 1, where the lead shock, the interface separating the discharging and ambient gases, the vortex ring and the inward-facing secondary shocks can be clearly seen.

† Present address: Department of Mechanical Engineering, University of Ottawa, 161 Louis Pasteur, Ottawa, Ontario K1N 6N5, Canada; matei@uottawa.ca
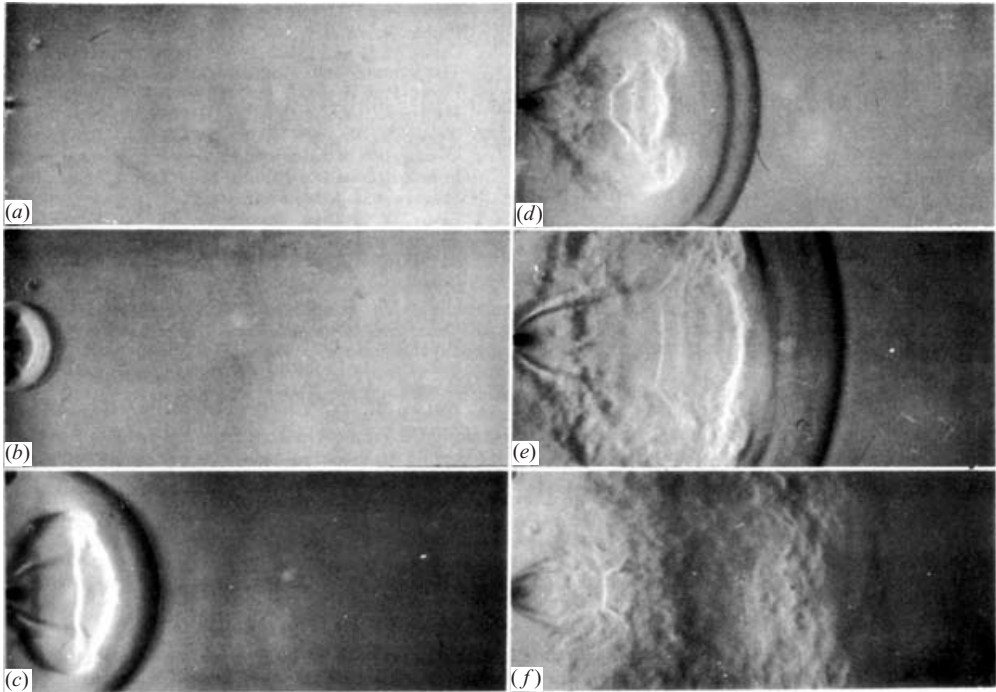
FIGURE 1. Shock transmission in Ar through a slit, giving rise to an under-expanded jet (adapted from Naboko *et al.* 1972).
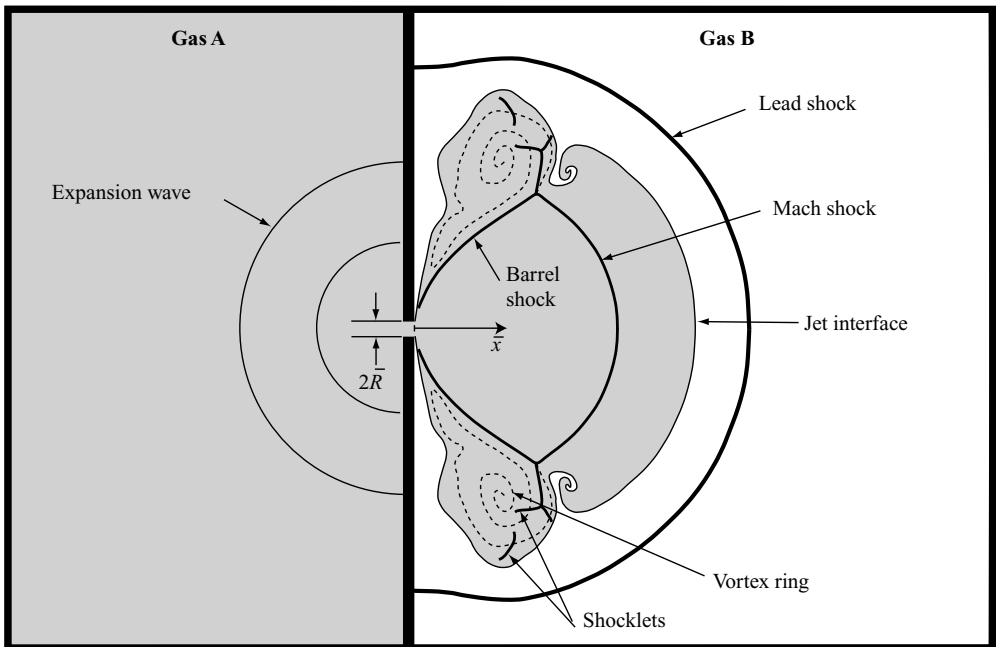

FIGURE 2. Physical set-up and sketch of the dynamically similar jet.

An explanatory sketch is shown in figure 2. The inner structure formed by the barrel shock and Mach stem resembles qualitatively the structure of steady under-expanded jets, which is established asymptotically as the lead shock decays to an acoustic wave in the far field (e.g. Ashkenas & Sherman 1964; Miller 1988; Maté *et al.* 2001).

Such unsteady or pulsed under-expanded jet sources are of interest in a number of applications. Examples are the starting of hypersonic nozzles in hypersonic wind tunnels or rocket engines, relaxation and non-equilibrium phenomena in molecular beams (see Campargue 1984 for review), population inversions in gasdynamic lasers (Hurle & Hertzberg 1965), transient hypersonic jet ejecta in astrophysical settings such extra-galactic jets (e.g. Falle 1991), and the accidental puncture of high-pressure vessels or lines. The last example has particular bearing on the explosion safety associated with the storage and handling of high-pressure gas fuels, such as hydrogen. Upon release of the high-pressure fuel jet into the surrounding oxidizing atmosphere, the driven shock can raise the air temperature by thousands of Kelvins, depending on initial fuel storage pressure (Dryer *et al.* 2007; Liu *et al.* 2005; Golub *et al.* 2005). Lighter fuels such as hydrogen are also more dangerous, as they drive stronger shocks. Ignition caused by the mixing of under-expanded hydrogen with shock-heated air was observed experimentally by Wolanski & Wojcicki (1973), Chaineaux, Mavrothalassitis & Pineau (1991), Groethe *et al.* (2005) and Dryer *et al.* (2007) and is currently being investigated theoretically and numerically (Radulescu & Law 2005). Preliminary numerical results were also recently presented in Golub *et al.* (2005) and Liu *et al.* (2005).

Although the steady jet has attracted much attention in molecular beam studies (Miller 1988; Campargue 1984), the details of the initial transient, particularly for large pressure ratios and strong shocks, are still poorly understood. This initial transient, during which the discharging and ambient gases mix at the interface via diffusion and cool through global expansions, is of prime importance to the fuel release problem and its ignition criteria (Radulescu & Law 2005). More generally, owing to the very fast evolution and intrinsic flow instabilities during the discharge, accurate measurements of the flow field are difficult to perform. Experimental investigations are usually limited to phenomenological descriptions based on schlieren-type photographs, which integrate along the line of sight and make an accurate appraisal of the three-dimensional flow field difficult (Buckmaster 1964; Naboko *et al.* 1977; Lacerda 1986; Golub 1994; Ishii *et al.* 1999). Numerical simulations are limited to weakly under-expanded jets of inviscid perfect gases (Ishii *et al.* 1999). Limited resolution did not allow capturing of the turbulent flow fields associated with the vortex rings observed experimentally (e.g. Naboko *et al.* 1974; Lacerda 1986), nor resolving diffusive effects at the contact surfaces. The numerical task is in general further complicated by the presence of chemical reactions and when transport processes are enhanced by turbulence. In the reactive under-expanded jet problem, a proper account of the ignition phenomenon at the mixing layer separating fuel and oxidizer can only be achieved via detailed calculations of the non-equilibrium diffusive mixing at the molecular scale. Such a detailed simulation of the entire problem from the large scales of the jet discharge to the molecular scales at the mixing interface would be extremely difficult with the present computational capabilities. A simpler approach to this problem is devised in the present study.

Owing to the complexity of the general jet discharge problem, the present study seeks to elucidate the flow field in two stages. First, we conduct numerical experiments on highly unsteady jets in order to determine the flow field and the physical processes involved during the jet release of high-pressure gases. Since we are interested in

the high Reynolds number limit, convective fluxes dominate over diffusive fluxes everywhere except in very thin layers around contact surfaces and shocks where large gradients are found. Away from these virtual discontinuities, the flow may be considered inviscid and in quasi-equilibrium, modelled by the Euler equations for a perfect gas. Secondly, we wish to model analytically the gasdynamic evolution of the interface separating the two gases and obtain the evolution of its velocity, pressure, temperature and density. This analytical result provides the varying boundary conditions for an analysis of the diffusive inner layers, which can be conducted separately on much smaller domains, and can be used to study the ignition process of the reactive jet.

The approximate solution obtained is based on Chernyi's boundary-layer method for hypersonic flows (Chernyi 1961), which exploits the limit of strong shocks obtained when the specific heat ratio approaches unity, also known as the Newtonian limit. The method has yielded very good results in the past for unsteady blast wave problems (see Chernyi 1961 and references therein). The present solution is based to leading order on the solution given by Chekmarev (1975) for a hypersonic pulsed spherical source. Its application to sonic jets, considered subsequently in Chekmarev & Stankus (1984) is modified by reviewing the formulation of the model. The method is then extended to higher orders using Chernyi's theory in order to obtain the evolution of the pressure, density and temperature at the interface as a function of time.

The paper first presents the numerical solution of highly under-expanded jets in detail. This is followed by the derivation of the analytical model for the evolution of the jet head surface, the estimation of the domain of validity of the model, and a comparison with the numerical results and available experimental data.

2. Physical set-up, governing equations and numerical technique

The physical set-up we are addressing is shown in figure 2. A high-pressure gas A enclosed by a thin wall is separated from an ambient gas B at much lower pressure. At $\bar{t} = 0$, the virtual interface separating the two gases at $\bar{x} = 0$ is removed, permitting the escape of the high-pressure gas through an aperture of radius $\bar{R}$. Here an overbar always denotes a dimensional quantity. We are considering the general problem where the aperture is either a long slit or round. The gases are assumed to be perfect. Very high Reynolds and Péclet numbers are assumed, such that viscous and diffusive effects are restricted to regions with high gradients, such as the interface between the two gases A and B, shock waves and vorticity layers. Away from these virtual discontinuities, we seek a gasdynamic solution of the flow-field evolution, which is governed by the Euler equations. Choosing pressure $\bar{p}$, density $\bar{\rho}$ and velocity $\bar{u}$ as dependent variables, the conservation of mass, momentum and energy can be written in dimensional form as

$$\frac{\partial \bar{\rho}}{\partial \bar{t}} + \nabla \cdot (\overline{\rho u}) = 0, \tag{2.1}$$

$$\frac{\partial (\bar{\rho} \bar{u})}{\partial \bar{t}} + \nabla \cdot (\overline{\rho u u} + \nabla \bar{p}) = 0, \tag{2.2}$$

$$\frac{\partial (\overline{\rho e})}{\partial \bar{t}} + \nabla \cdot ((\overline{\rho e} + \bar{p}) \bar{u}) = 0, \tag{2.3}$$

where $\bar{e}$ is the total energy (internal and kinetic)

$$\bar{e} = \frac{\bar{p}/\bar{\rho}}{\gamma - 1} + \frac{1}{2} \bar{u}_l \bar{u}_l, \tag{2.4}$$

Initial conditions		One-dimensional shock tube problem solution					Similarity parameters	
p_{Ao}/p_{Bo}	ρ_{Ao}/ρ_{Bo}	M_{S1}	p_i/p_{Bo}	ρ_{Ai}/ρ_{Bo}	ρ_{Bi}/ρ_{Bo}	u_i/a_{Bo}	ρ_{Bo}	a_{Bo}
88.1	6.08	4.35	21.9	2.25	4.75	3.43	0.260	0.288
337	23.2	6.03	42.3	5.27	5.27	4.89	0.0679	0.288
700	48.3	7.01	57.2	8.07	5.45	5.73	0.0327	0.288

TABLE 1. Parameters for the three sets of simulations.

where the subscript l represents the lth component of the velocity vector, and a repeated index follows the summation rule over the values taken by the index; γ is the isentropic exponent and the sound speed is given by

$$\bar{a}^2 = \gamma \bar{p}/\bar{\rho}. \tag{2.5}$$

The same equations apply for both gases A and B, which are characterized by different isentropic exponents γ_A and γ_B. The molecular weights of gases A and B can also differ; however the gasdynamic solution to the problem posed above does not depend explicitly on molecular weights. The molecular weights $\bar{W}$ only affect the final temperature field, which is computed from the final gasdynamic solution from the ideal gas equation,

$$\bar{T} = \frac{\bar{W}\bar{p}}{\bar{R}_u\bar{\rho}}, \tag{2.6}$$

in each respective gas, provided the boundary surface separating the two gases is also known. $\bar{R}_u$ is the ideal gas constant.

For simplicity, the numerical simulations performed in this study are restricted to gases which share the same isentropic exponent γ, such that we solve only one set of governing equations for both gases. The case of gases with different molecular weights addressed here does not pose any difficulty, and is achieved implicitly by setting the correct initial density and pressure on each side of the partition. The interface between the two gases is deduced by convecting an inert scalar α, set to 0 in gas A and 1 in gas B. The evolution of the α field is given by

$$\frac{\partial(\bar{\rho}\alpha)}{\partial\bar{t}} + \nabla \cdot (\bar{\rho}\bar{u}\alpha) = 0. \tag{2.7}$$

The finite numerical diffusion leads to a slight smearing of the scalar at the interface; the interface location was hence assumed to correspond to the position where $\alpha = 0.5$. Note that values of α differing from 0 or 1 is a pure artifact due to the diffusion of numerical errors from the discretization of the equations, since this is not a solution of (2.7) and the given initial conditions. Knowledge of the approximate position of the interface permits us to use (2.6) to obtain the temperature field in each gas.

The parameters chosen in the simulations correspond to the expansion of hydrogen gas in air. We take $\gamma = 1.4$ for both diatomic gases for simplicity. Given the molecular weights of hydrogen and air ($\bar{W}_A = \bar{W}_{H_2} = 2$, $\bar{W}_B = \bar{W}_{air} = 29$) and using (2.6), the initial pressures and densities are set such that the temperatures are initially equal in both gases. Table 1 gives the initial conditions for the three sets of simulations considered in both the slit jet and round jet geometries.

In view of the subsequent analysis, the most convenient non-dimensionalization of the governing equations is obtained by taking the scales imposed by the sonic throat developed near the orifice in gas A as reference. For a steady isentropic expansion

from the stagnation state of gas A, we obtain (Liepmann & Roshko 2001)

$$\bar{a}_{Ac} = \bar{a}_{Ao}\left(\frac{2}{\gamma_A + 1}\right)^{1/2}, \tag{2.8}$$

$$\bar{\rho}_{Ac} = \bar{\rho}_{Ao}\left(\frac{2}{\gamma_A + 1}\right)^{1/(\gamma_A-1)}. \tag{2.9}$$

The subscripts o and c denote the stagnation condition and the choked state respectively. We thus choose the puncture radius $\bar{R}$ as reference scale, $\bar{\rho}_{Ac}$ as reference density and $\bar{a}_{Ac}$ as reference speed. The non-dimensional variables hence become

$$x \equiv \frac{\bar{x}}{\bar{R}}, \quad u_l \equiv \frac{\bar{u}_l}{\bar{a}_{Ac}}, \quad \rho \equiv \frac{\bar{\rho}}{\bar{\rho}_{Ac}}, \quad p \equiv \frac{\bar{p}}{\bar{\rho}_{Ac}\bar{a}_{Ac}^2} = \frac{\bar{p}}{\gamma_A \bar{p}_{Ac}}, \quad t \equiv \frac{\bar{t}\bar{a}_{Ac}}{\bar{R}}. \tag{2.10}$$

The governing equations (2.1) to (2.3) remain unchanged in terms of the non-dimensional variables. In the new variables, the aperture radius becomes unity. The solution presented henceforth will be in terms of the variables defined in (2.10), with symbols with an overbar always denoting dimensional variables.

Owing to the symmetry of the problem, the computational domain consists only of the upper half (see figure 2). The domain also comprises the gas A reservoir, into which unsteady expansions propagate. In all simulations presented, the external boundaries of the computational domain are placed sufficiently far to not influence the flow field. The two compartments are separated by a thin solid wall, with a thickness nominally set to 0.125 (except where otherwise noted). The origin of the horizontal x-axis in figure 2 is at the right-hand surface of the wall.

The hierarchical adaptive code μCobra, described in Falle & Giddings (1993) and Falle (1991), is used to solve the governing equations in two-dimensional Cartesian and axisymmetric coordinates, corresponding respectively to slit and round jets. The code uses a second-order Godunov scheme in which the second-order Riemann problems are constructed from the primitive variables using a quadratic averaging function. An exact Riemann solver is used wherever necessary and a linear solver elsewhere. The code uses a hierarchical series of Cartesian grids $G^0, \ldots, G^M$, so that grid G^M has mesh spacing $\Delta x = h/2^M$, where h is the mesh spacing on the base grid G^0. Grids G^0 and G^1 cover the entire domain, but the more resolved grids only occupy regions where increased resolution is required. Refinement is controlled by comparing the solution of each conserved variable and also their rates of change on grids G^m and G^{m-1}. If either of these errors is greater than the given tolerances, the grid is refined to level G^{m+1}, $m + 1 \leqslant M$. These conditions can be used to ensure that regions where the flow is changing rapidly, e.g. shocks, are always resolved to the highest level. The code was extensively tested on various multi-dimensional compressible flow problems and has been used successfully to investigate detonation waves (Sharpe 2001).

In the numerical scheme, artificial diffusion was added to the momentum and energy fluxes determined from the Riemann solution in order to suppress the Quirk instability (Quirk 1992) and to remove the entropy oscillations behind slowly moving shocks, as described in Falle & Komissarov (1996). The viscous stress is defined in terms of the left and right states in the Riemann problem and the local sound speed:

$$\tau^{ij} \propto \rho a \left(\phi_L^i - \phi_R^i\right), \tag{2.11}$$

where ϕ_L^i and ϕ_R^i are the re-constructed primitive variables (velocity u and temperature T in the momentum and energy conservation respectively) at the cell interface in the Riemann problem of the j-direction. Falle & Komissarov (1996) show that in smooth

regions, where the solver is second-order accurate, the resulting diffusivities become proportional to the square of the grid spacing Δx. The highest numerical diffusivities however occur in regions of the flow where discontinuities are present, where the scheme becomes first-order accurate. The resulting kinematic viscosity and heat diffusivity become proportional to the grid spacing Δx (Falle & Komissarov 1996). In the non-dimensional scales defined in (2.10), the resulting numerical Reynolds number Re_{num} is simply the inverse of the diffusivity and becomes

$$Re_{num} = \left(0.2 \left(\frac{a}{a_{Bo}} \right) \Delta x \right)^{-1}. \tag{2.12}$$

where a is the local sound speed and a_{Bo} (the initial sound speed in gas B) is given in table 1 for the present running conditions. Since the grid spacing Δx ranges between 1 and 1/256 in the present simulations (see below) and taking characteristic values of $a \sim 1$, the minimum Reynolds number ranges from approximately 1 to 400 near contact layers and shock discontinuities. These Reynolds numbers are commensurate with experimental values corresponding to low initial pressures in the receiver gas B on the order of 1 Pa, but are a few orders of magnitude lower than the values obtained for jets issuing in gases at pressures on the order of 10^3–10^5 Pa (Korobeishchikov, Zarvin & Madirbaev 2004), which are encountered in practical applications and jet experiments. In this sense, the solutions presented below are much more diffusive than would be encountered in the situation of a pressurized hydrogen jet emerging into atmospheric pressure.

3. The flow field

3.1. *Initial jet establishment*

The early development of the flow field for a slit geometry immediately after the release of the high-pressure gases is illustrated in figure 3 in terms of the pressure gradient field. The figure shows the one-dimensional expansion wave established at the axis ($y = 0$), the diffraction of the shock formed around the corner in the positive x-direction and the diffraction of the expansion wave propagating in the negative x-direction. The initial condition is ($p_{Ao}/p_{Bo} = 337$), corresponding to matched densities at the interface after the gas release, as obtained analytically from the one-dimensional shock tube solution. The solution was obtained on a uniform grid with mesh spacing $h = 1/256$ (i.e. 256 grid points per aperture radius $\bar{R}$). Upon release of the gases, an initially Mach 6.0 planar shock wave is driven by the expanding gases along the axis, in very good agreement with the well-known solution for the one-dimensional shock tube problem (Liepmann & Roshko 2001). Results of the shock tube solution are listed in table 1 for the cases considered. Note that the initial pressure ratio p_{Ao}/p_{Bo} is sufficiently high that the flow at the tail of the one-dimensional rarefaction wave at the axis is supersonic and the tail moves in the positive x-direction.

The lateral relaxation is more complicated than the well-known problem of shock diffraction (Skews 1967) owing to the presence of the one-dimensional shock tube expansion and the interaction of two centred waves associated with the two corners. First, the lateral diffraction of the shock wave is not influenced by these non-idealities at early times. The rapid lateral expansion of the gases around the corner is qualitatively similar to the multi-dimensional shock tube problem (Brode 1959; Boyer 1960; Friedman 1961) where gases impulsively expand, such as from a pressurized sphere. The signature of this multi-dimensional expansion is the secondary shock
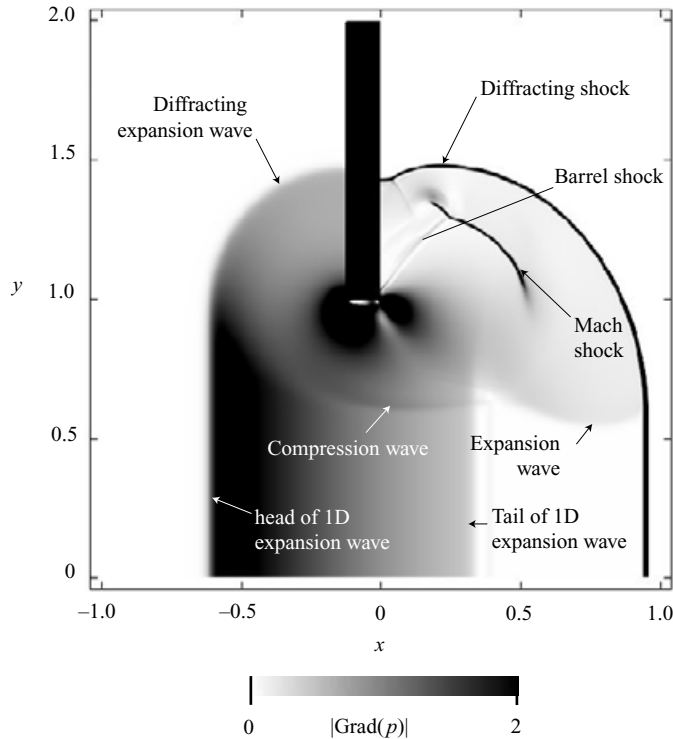
FIGURE 3. Pressure gradient field of the initial flow field of a slit jet at $t = 3.71 \times 10^{-2}$.

wave, clearly seen in the pressure gradient fields as the initial portion of what will become the Mach shock of the jet and the lateral barrel shock (see figure 2). The physical explanation for these secondary shocks is that a curved, geometrically imploding expansion wave reduces the pressure at a faster rate than a corresponding diverging curved shock, hence an inward moving weak shock wave is required to match the pressures (Friedman 1961). The secondary shock initially appears near the corner, where the gases are expanding in multiple dimensions. The inward-facing Mach shock is convected outwards by the supersonic outflow while the barrel shock remains attached to the expansion corner. Near the jet axis, where initially the problem is purely one-dimensional, this secondary shock is initially absent.

The presence of the one-dimensional unsteady shock tube expansion centred at $x = 0$ and its diffraction around the second corner at $x = -0.125$ complicates the flow field at early times and makes it non-self similar, owing to the length scale of the wall thickness. The diffraction of the one-dimensional expansion wave around the left-hand corner leaves a zone of higher pressure behind. At subsequent times, this weak train of compression waves reflects on the axis and propagates in the region of decaying density, catching up to the main diffracting shock. This latter evolution is illustrated in figure 4, which shows the distributions of density, pressure gradient and scalar α at three successive times. For this calculation, we have used a base grid G^0 with a mesh spacing of $h = 1/16$ and $M = 4$ resolution levels, yielding an equivalent grid spacing of $1/256$ for the most refined grid G^4. The weak train of compression waves, clearly seen in the second frame, is first propagating upwards. These waves preferentially amplify in the region to the left of the Mach shock, where the density is decaying. Owing to the density gradient, the compression waves amplify to form
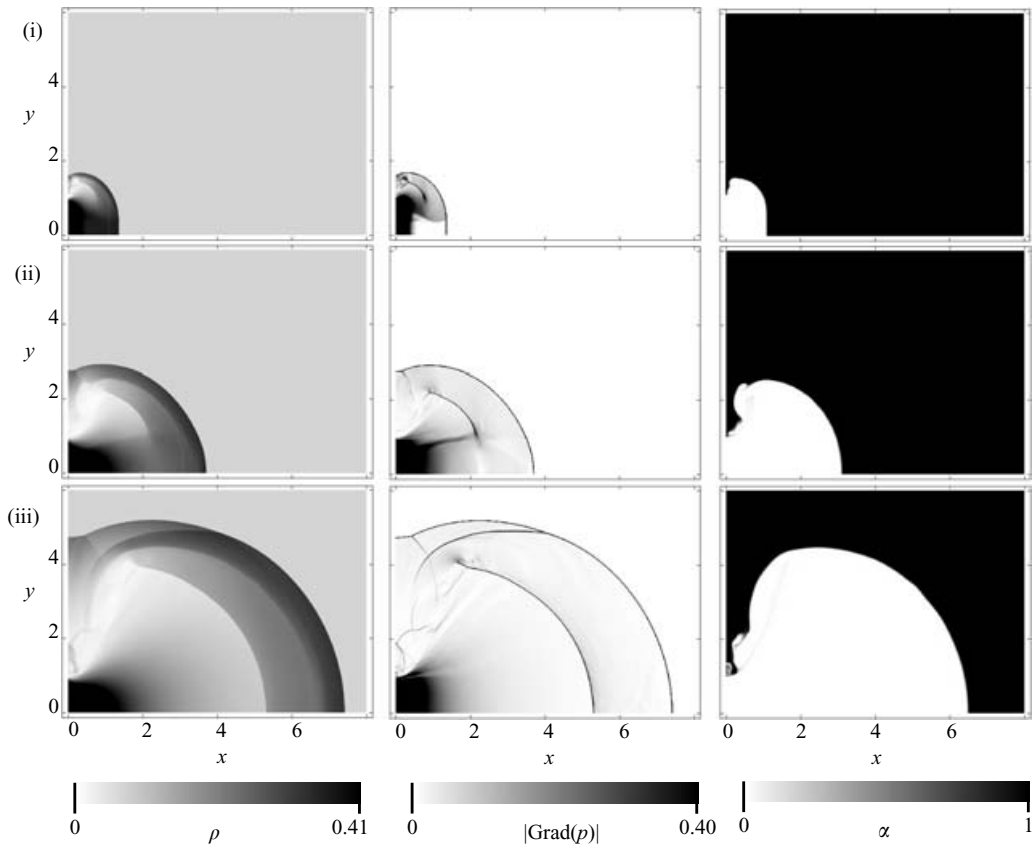
FIGURE 4. Density, pressure gradient and passive scalar α flow fields of a slit jet
at (i) $t = 0.0529$, (ii) 0.15 and (iii) 0.333.

a shock. In the last frame, part of it has overtaken the main shock near the front, and the other part has just traversed the lateral contact surface between the ejected and shocked gases. This interaction further disrupts the vorticity layer on the sides of the jet. Figure 4 also illustrates how the initial transient gasdynamics associated with the lateral relaxation of expansion waves transform the flow field into the typical jet structure illustrated in figure 2. Note that at these times scales in the observation, the flow field is not self-similar. The length scale of the aperture opening introduces the lateral relaxation of the flow.

The influence of the lateral relaxation on the flow field along the jet axis $y = 0$ is shown in figure 5. The pressure, density and axial velocity profiles are shown at the same time as the sequence illustrated in figure 4. The first profile, obtained before the onset of multi-dimensional effects, is found to be in excellent agreement with the ideal shock tube solution. As the multi-dimensional relaxation progresses, the parameters near the aperture approach the sonic conditions of the developing sonic throat. Away from the aperture, the establishment of the Mach shock is clearly seen. The expansions closer to the aperture are stronger due to the higher volumetric expansion per unit time and the gases acquire higher velocities. As a result, the pressure and density drop faster than can be accommodated by the leading shock decay and rear-facing compression waves give rise to the secondary shock.
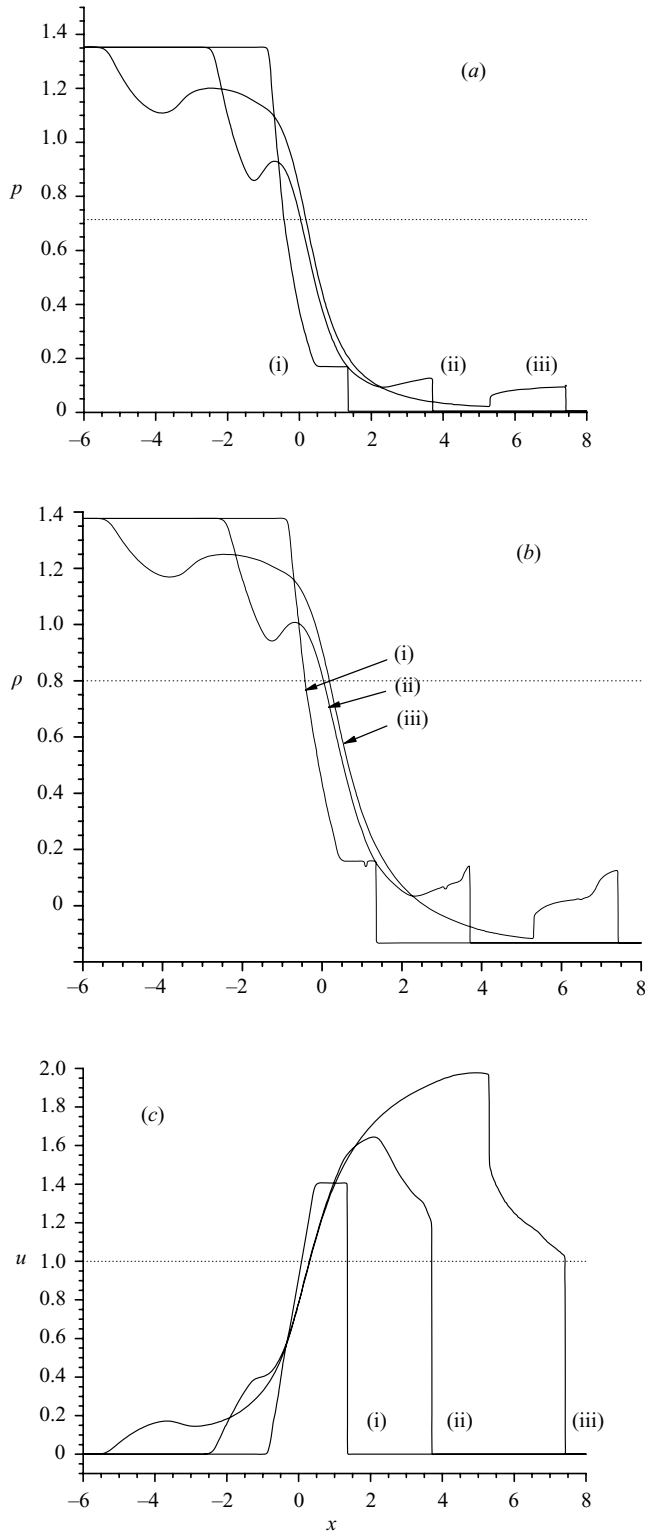
FIGURE 5. Pressure (*a*), density (*b*) and axial velocity (*c*) profiles along the axis $y = 0$ corresponding to the times illustrated in figure 4; dotted lines represent the conditions at a virtual sonic throat.
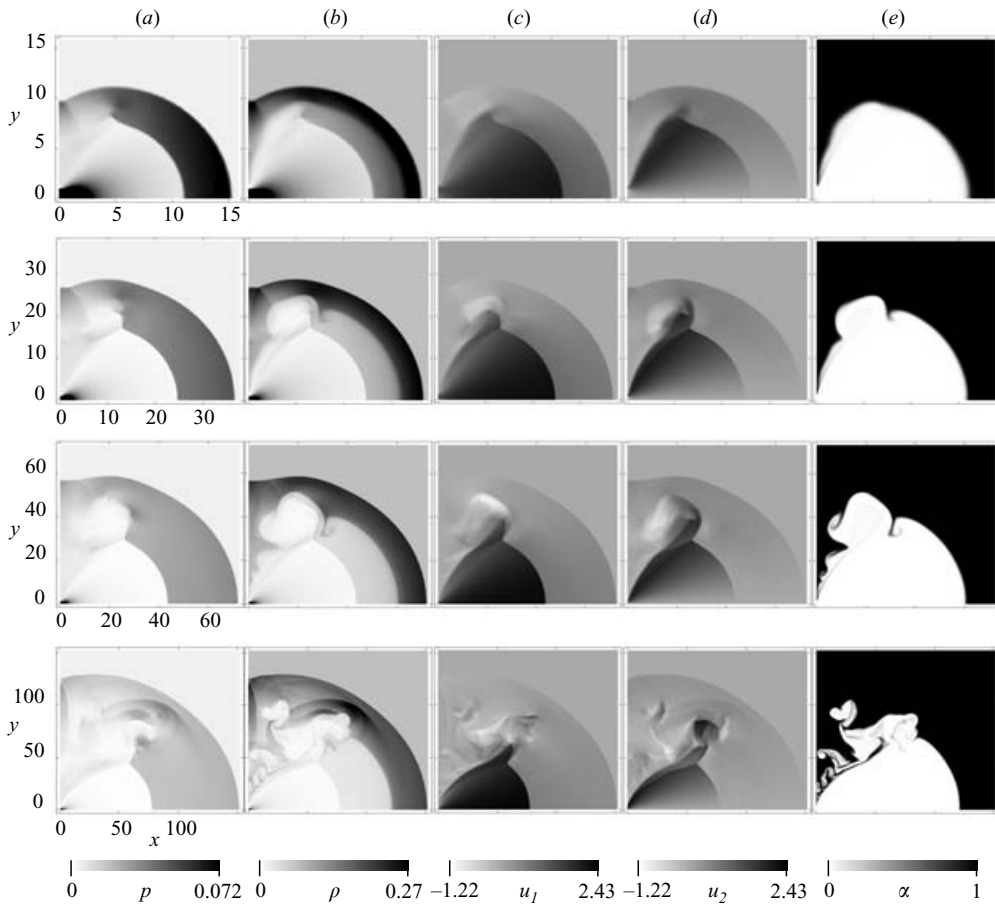
FIGURE 6. Pressure (*a*), density (*b*), axial velocity (*c*), transverse velocity (*d*) and passive scalar α (*e*) flow fields in a slit jet at $t = 0.766$, 2.19, 5.03 and 12.8.

3.2. *Dynamically similar regime*

The subsequent evolution of the pressure, density, velocity components and inert scalar α is shown in figure 6. Owing to the larger domain, the base grid mesh spacing was increased to 1 and we used 3 resolution levels, such that the most resolved grid had a mesh spacing of $1/8$. At these later times, the global morphology of the flow field appears dynamically similar, with growing leading curved shock, contact surface and the secondary shock system formed by the barrel and Mach shocks. The flow field elements are labelled in the sketch of figure 2. The flow field is not strictly similar. For example, the ratios between the inner and outer shock radii or between the interface and shock radii evolve slowly while the scales change by more than an order of magnitude. The apparent similarity is in good accord with the fact that the scale of the aperture is now negligible compared with the characteristic dimensions of the flow field. In this sense, the flow field achieves a symmetry centred around the vanishing size aperture.

Small-scale instabilities are found to appear in the lateral flow field associated with the re-circulation flow in the vortex rings. The flow is further complicated by a system of shocklets at the periphery of the vortex ring, one of which is the extension of
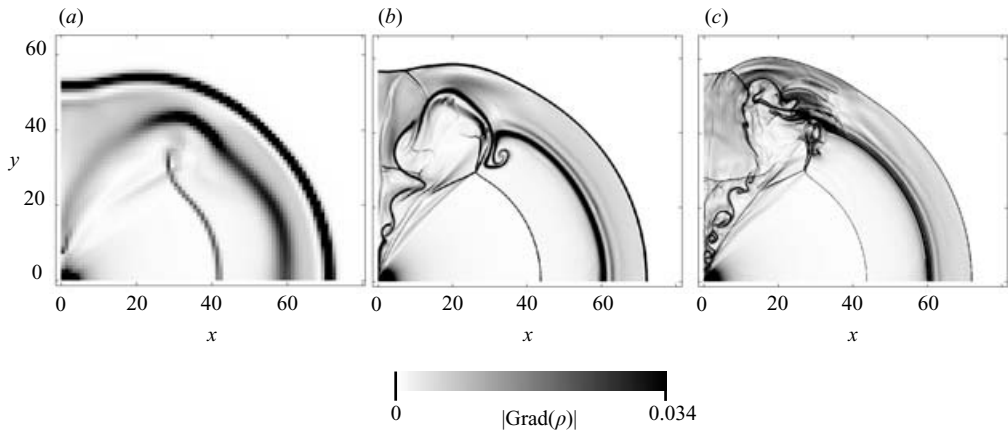
FIGURE 7. The density gradient flow field in a slit jet at $t = 5.03$ with different resolutions: (a) 1 grid point/$\bar{R}$, uniform grid; (b) 8 grid points/$\bar{R}$, 3 refinement levels; and (c) 32 grid points/$\bar{R}$, 5 refinement levels.

the reflected shock at the Mach stem and barrel shock interaction, which bifurcates in the vortex ring. Similar features have been obtained in numerical simulations by Ishii *et al.* (1999) for weaker jets. The interaction of the shocks with the expanding re-circulating flow makes an accurate reconstruction of the exact flow field difficult. These small-scale details of the flow field within the vortex ring were found to change as the grid was refined. For example, the density gradient field obtained with different resolutions is shown in figure 7. The results illustrate well the change in the coherent structures along the interface separating the two gases with increasing resolution. Characteristic Kelvin–Helmholtz billow structures form on the interface separating the downward-moving re-circulating gas A and gas B at a faster rate with increasing resolution. As time progresses, these billows interact nonlinearly and are deformed and folded by the passage of shocks. Owing to the presence of large density gradients at the interfaces, the shock interactions lead to vorticity production by the baroclinic interaction of misaligned pressure and density gradients.

Such instabilities involving multi-dimensional expansions, shocks, density interfaces and regions of high vorticity would require the solution of the true non-equilibrium gasdynamics involving transport mechanisms at small scales. Since we are solving the inviscid Euler equations, the damping of the flow instabilities relies only on the numerical diffusion, which is controlled by the resolution level. Owing to these limitations, the small scales of the lateral part of the jet can only converge if the dissipation is correctly modelled and independent of resolution, which is not the case here. Nevertheless, the simulations do show the wide range of phenomena expected to play a role as the Reynolds number increases. Note however that the real Reynolds numbers are still much higher than the numerical ones, and phenomena of increasing complexity are expected.

Although the lateral flow field does not converge, the laminar jet head dynamics has converged to the correct solution. Figure 8 shows the pressure, density, velocity and scalar α along the axis for the three resolution levels shown in figure 7. The flow field near the axis is very well captured at different resolution levels, even at the lower resolution with mesh spacing of 1.

The complete evolution of the pressure, density and velocity profiles along the jet axis is shown in figure 9. The profiles of figure 5 are also shown. The flow field can
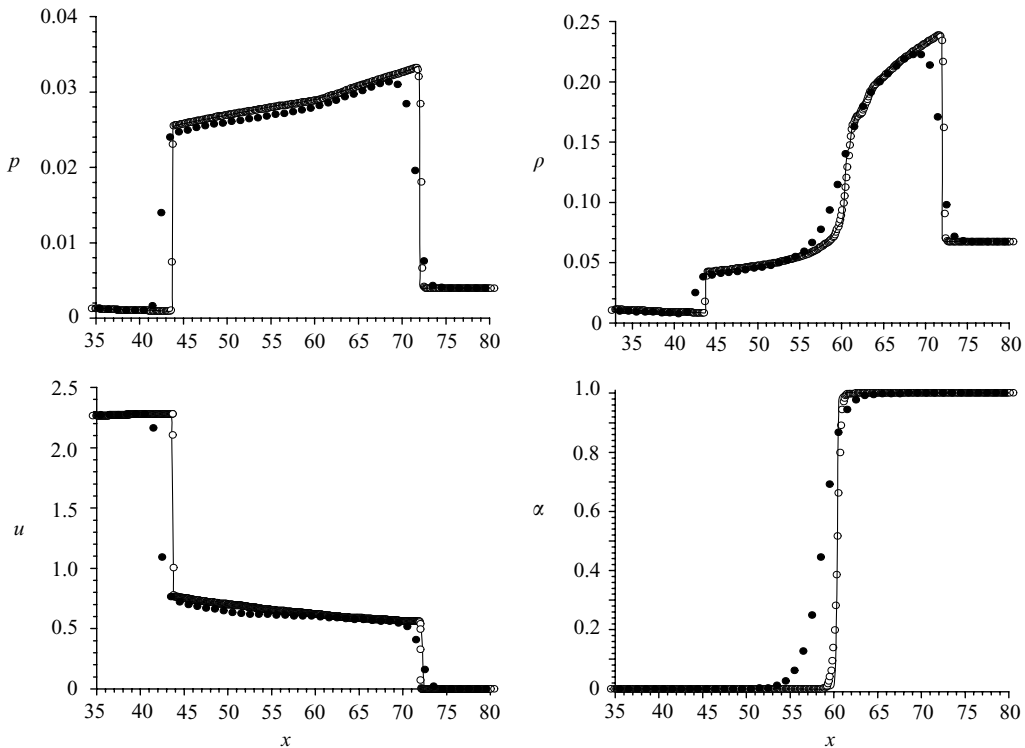
FIGURE 8. Pressure, density, velocity and scalar α profiles along the flow axis $y = 0$ correspond-ing to the different resolution levels of figure 7: line, 32 pts/$\bar{R}$; open circle, 8 pts/$\bar{R}$; closed circle, 1 pt/$\bar{R}$.

be separated into two parts. First, the expansion from the aperture to the inward-facing shock becomes steady, and a sonic throat is developed at $x \approx 0.3$. As the flow from the source to the secondary shock follows the steady expansion, the layer of gas between the main and secondary shocks containing the gas interface is continuously changing. While the main shock becomes progressively weaker owing to its geometrical divergence, the inward-facing shock becomes stronger as it propagates into expanding gas (although being convected outwards). Interestingly, the interface between the two gases develops an inflection point in the density profile. This feature will be discussed in the framework of the analytical model developed below.

3.3. *Late stages of jet formation*

The late stages of the slit-jet establishment are illustrated in figure 10 in terms of the pressure, density and scalar α fields at four successive times for the matched-density jet considered above. Owing to the much larger domains necessary to monitor the late evolution, the calculations were performed on a uniform grid with a grid spacing of unity. The wall thickness separating the two gases was also set to 1. The global morphology of the late jet is in good agreement with the experimental photographs of figure 1. The calculations further capture a number of interesting phenomena of increasing complexity. First, the vortex rings, easily located by the regions of low pressure, appear to be radiating a complex system of weak shocklets. These are also clearly visible in the schlieren photographs of the late time evolution of jets of light gas into heavier gases taken by Lacerda (1986) and in the high-pressure jets of Naboko
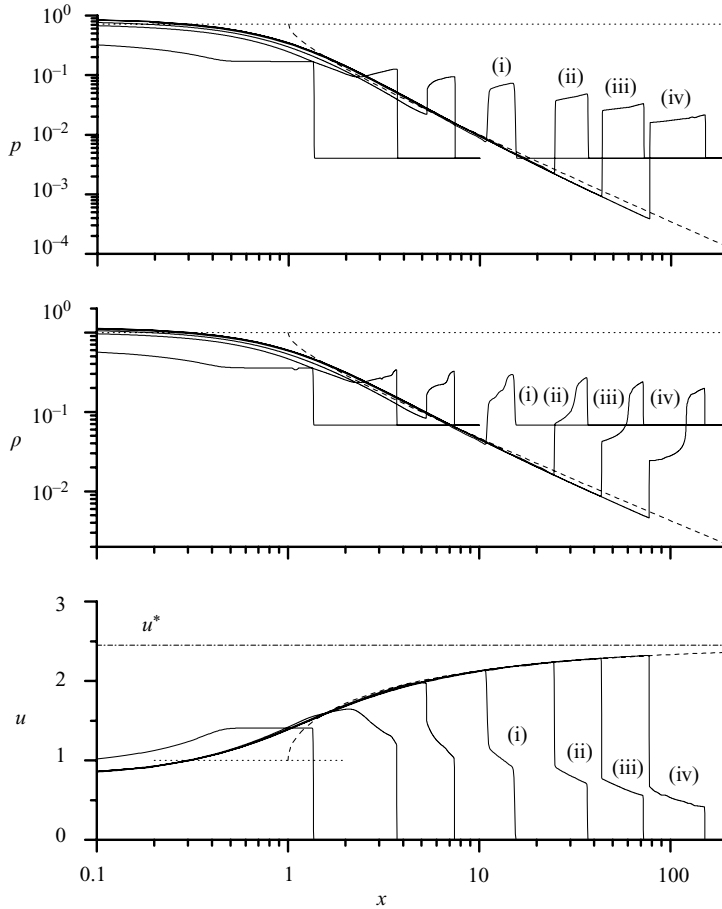
FIGURE 9. Pressure, density and axial velocity along the slit-jet axis $y = 0$ for the four times illustrated in figure 6 (successive solutions denoted by (i) to (iv); also shown are the profiles of figure 5: dotted line, virtual throat condition; broken line, exact solution of symmetric expansion from a choked source of dimension $\Lambda = 1$; dotted-broken line, maximum permissible expansion velocity.

et al. (1974) and heated jets of Golub (1994). The mechanism for the formation of this acoustic radiation is still unclear, although it appears to be associated with the transient rapidly expanding regions of flow, individually isolated via instabilities in the vortex rings. Simultaneously with these complicated shock systems, the interface between the two gases becomes significantly more convoluted. The flow field acquires all the basic attributes of compressible turbulence, with shock, vorticity and density layer interactions. Based on the results of the resolution study shown in figure 7 performed at earlier times of the jet evolution, the morphology of the jet is likely to become much more convoluted than captured numerically with the present limited resolution. This is also anticipated based on the experimental observations made by Golub (1994) regarding the intense turbulent structure of such jets.

Inspection of the global morphology of the jet also shows that the layer of gas between the Mach shock and lead shock is also significantly disturbed and shows density variations. This is unlike the earlier stages of the jet evolution, in which the frontal part of the jet was very weakly affected by the lateral vortex rings. A tentative qualitative picture of this effect can be constructed based on the temporal evolution
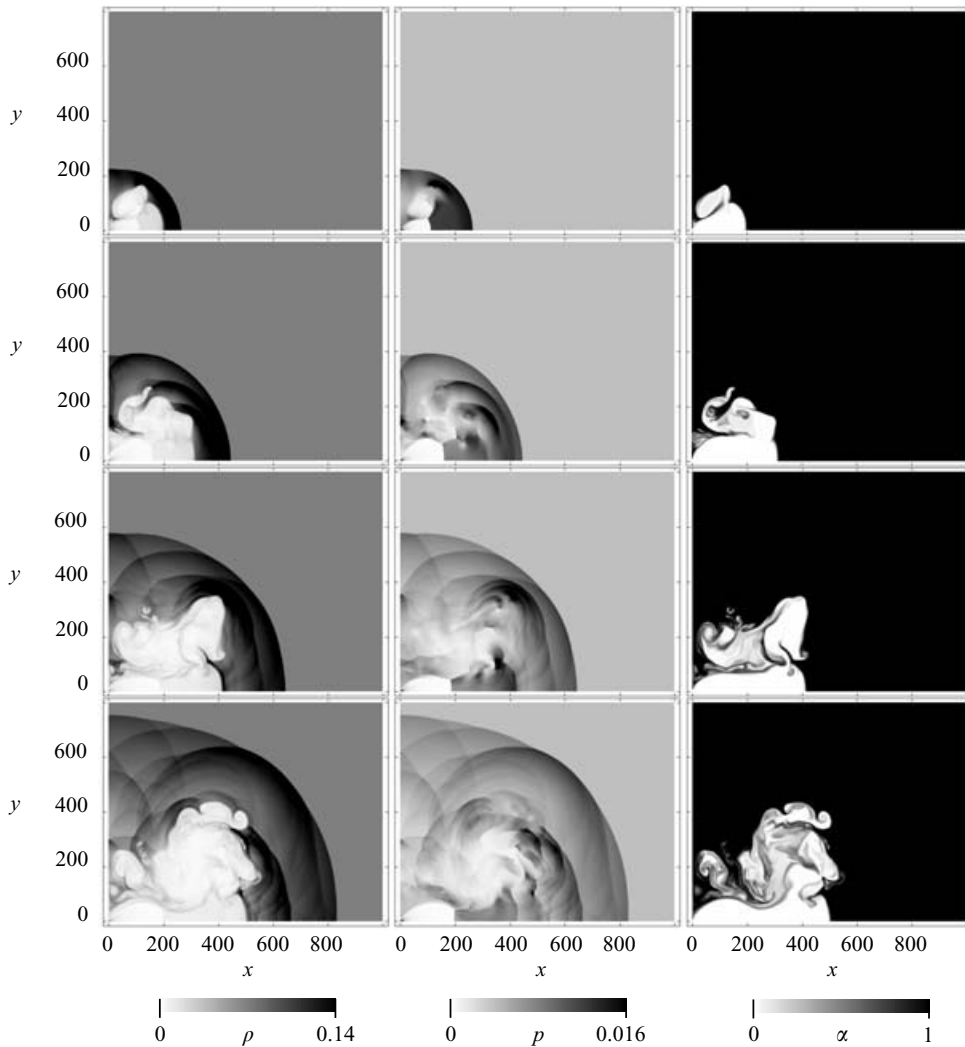
FIGURE 10. Density, pressure and scalar α evolution at the late stages of the slit-jet formation illustrating the acoustic radiation from the lateral vortex rings; successive frames taken at $t = 26.6$, 51.5, 81.2 and 111.

of the global jet morphology. Taking figure 10(*c*) for example, we see that the global structure of the jet cross-section appears to be first diverging, than re-converging, to finally diverge again. This is due to an initial over-expansion of the jet, followed by a subsequent re-compression, and re-expansion, typical of pulsed radially expanding flows (e.g. Brode 1959). This effect is also visible in the photographs of Naboko *et al.* shown in figure 1. Golub (1994), Ishii *et al.* (1999) and Lacerda (1986) illustrate the sequence of expansions and re-compressions at the very late stages of weaker jets with multiple consecutive Mach stems. These were observed once the leading shock has travelled a long distance compared to the location of the first Mach shock.

3.4. *Round jet evolution*

So far, we have considered the evolution of a two-dimensional slit jet. The discussion presented also applies qualitatively to the round jet. We shall briefly present the
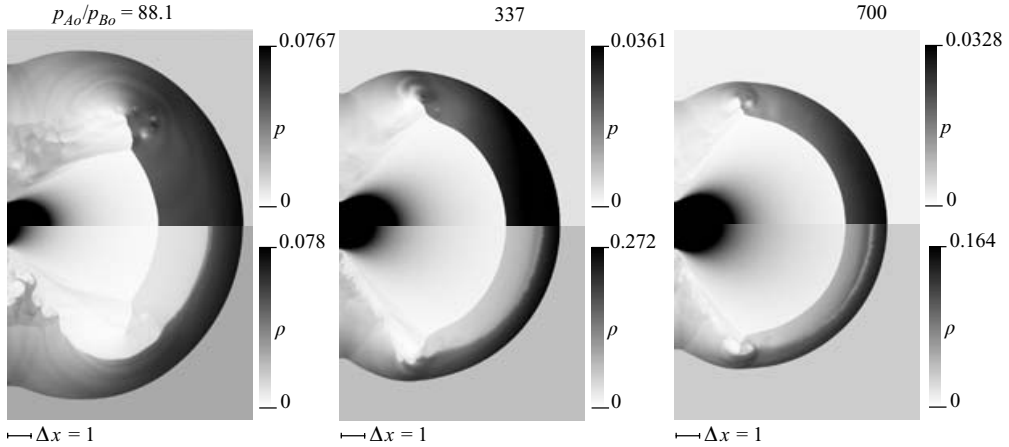
FIGURE 11. Pressure (upper half) and density (lower half) fields in round jets of initial strengths $p_{Ao}/p_{Bo} = 88.1$, 337 and 700 taken at times $t = 9.54$, 6.19 and 4.98 respectively such that the interface separating driven and driver gases is at the same x location.

numerical solutions for the round jet, computed with an axisymmetric regularly spaced base grid with a mesh spacing of $h = 1/16$ using 4 refinement levels, such that the most refined level has a grid spacing of $1/256$. Figure 11 shows the pressure and density distributions for the three different jet strengths listed in table 1 at a time when the jet interface is at the same location in the three cases. The flow details are qualitatively the same as described above. The weaker jet appears to have dynamically evolved to a much later morphology than the stronger jets, as indicated by the smaller diameter of the Mach shock and the thicker gas layer between the Mach and lead shocks. The scaling of the jet dynamics and morphology will be demonstrated below in terms of the model developed.

Figure 12 shows the pressure and density distributions along the jet axis corresponding to the profiles of figure 11. We see that in spite of the jet differences, the expansion established between the aperture and the first inward-facing shock acquires a unique steady structure, as was also verified from profiles obtained at later times.

4. Jet model

4.1. *An equivalent one-dimensional flow field with line or point symmetry*

The numerical solutions of the jet have revealed that a steady expansion wave is developed between the sonic throat at the aperture and the inward-facing shock. Since the flow in the steady expansion is bounded by the inward-facing shocks, it is outside the domain of influence of the exterior flow field and the steady expansion occurs as an expansion of accelerating gas into vacuum. If we are interested in the dynamics occurring at scales much larger than the aperture, we can attempt to model the flow field along the jet axis as a point- or line-symmetric flow field originating from a sonic source of a dimension commensurate with the aperture dimension. For the slit jet, the source would be a long cylinder, while for the round jet, the source would be a sphere. To first approximation, the location of the centre of symmetry of the source can be made to coincide with the plane of the aperture. This idealization is shown schematically in figure 13. We hence replace the original jet problem with a one-dimensional analogue of a pulsed sonic source. The pulsed
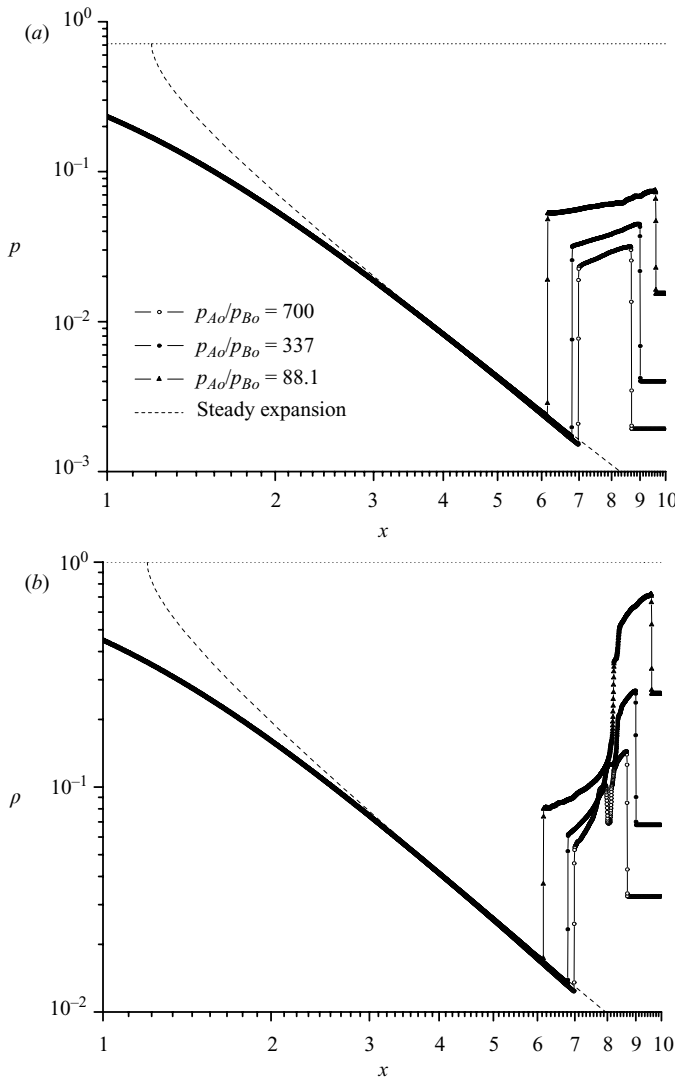
FIGURE 12. Pressure (*a*) and density (*b*) along the jet axis for the three jet conditions shown in figure 11; dotted line; virtual throat condition; broken line, exact solution of symmetric expansion from a choked source of dimension $\Lambda = 1.2$.

source will yield a system comprising the main shock (S_1), the inward secondary shock (S_2) and the contact surface (i), analogous to the jet-driven shocks and jet boundary (Chekmarev & Stankus 1984). Our aim is to obtain a solution of this gasdynamic problem and provide the link to the original jet problem.

The sole matching parameter in the above model is the size of the symmetric source, to be adjusted such that the ensuing expansion from the model source matches the expansion of the real three-dimensional jet along the jet axis. The solution for a one-dimensional steady expansion from a sonic source, emanating from the surface of a cylindrical/spherical source centred at $x = 0$ and of radius Λ can easily be derived from the steady conservation equations of mass and energy (see for example
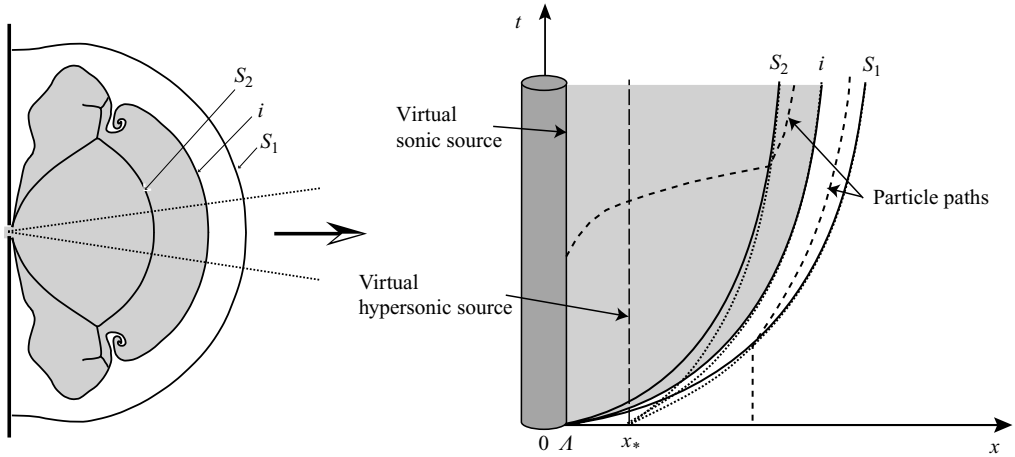
FIGURE 13. Dynamics of the jet axis flow-field evolution modelled by a one-dimensional pulsed sonic source of radius Λ and a virtual hypersonic source of radius x_*.

Liepmann & Roshko 2001 or Bochkarev, Rebrov & Chekmarev 1969), yielding

$$a^2 = \left(\frac{2}{\gamma_A + 1} + \frac{\gamma_A - 1}{\gamma_A + 1} M^2 \right)^{-1}, \tag{4.1}$$

$$\rho = \left(\frac{2}{\gamma_A + 1} + \frac{\gamma_A - 1}{\gamma_A + 1} M^2 \right)^{-1/(\gamma_A - 1)}, \tag{4.2}$$

$$p = \frac{1}{\gamma_A} \left(\frac{2}{\gamma_A + 1} + \frac{\gamma_A - 1}{\gamma_A + 1} M^2 \right)^{-\gamma_A/(\gamma_A - 1)}, \tag{4.3}$$

$$u = Ma = M \left(\frac{2}{\gamma_A + 1} + \frac{\gamma_A - 1}{\gamma_A + 1} M^2 \right)^{-1/2}, \tag{4.4}$$

$$\left(\frac{x}{\Lambda} \right)^j = \frac{1}{\rho u} = \frac{1}{M} \left(\frac{2}{\gamma_A + 1} + \frac{\gamma_A - 1}{\gamma_A + 1} M^2 \right)^{(\gamma_A + 1)/2(\gamma_A - 1)}. \tag{4.5}$$

where M is the local Mach number of the flow and j is the geometric index ($j = 1$ or 2 for axial symmetry or spherical symmetry, respectively). By trial and error, we found that a very good choice for the size of the choked source is $\Lambda = 1$ for slit jets and $\Lambda = 1.2$ for round jets for the conditions considered in the numerical simulations. The resulting steady expansion given from the above relations is shown in figure 9 for the slit jet and figure 12 for the round jet along with the numerical results, illustrating the excellent agreement. The fact that $\Lambda \sim 1$ yields a good agreement can also be argued on a physical basis, since the characteristic dimension of the pulsed sonic source should be of the same order as the radius of the aperture in the multi-dimensional jet release. We emphasize that the replacement of the multi-dimensional flow field with an equivalent one-dimensional flow field with cylindrical or spherical symmetry and dimension Λ is the sole empirical treatment of the problem, since a rigorous asymptotic approach seems difficult in view of the complexity of the three-dimensional flow field at early times.

4.2. *Model for the unsteady development of the interface and shocks*

It is useful to replace the problem of a sonic pulsed source with the problem of a hypersonic pulsed source (treated in Chekmarev 1975), which can be solved much

more easily. The idealization is shown schematically in figure 13. In the new problem of a pulsed hypersonic source (Chekmarev 1975), we assume that at time zero, a source of radius x_* is suddenly turned on with constant hypersonic velocity, which is maintained subsequently. Our aim is to obtain a solution to this new gasdynamic problem in the far field $x \gg x_*$ and to relate the source radius x_* and parameters of the source p_*, ρ_*, u_* to the parameters (which are unity by our non-dimensionalization) of the choked source of radius Λ and hence to our original jet problem. Such a matching is lacking in the formulation of Chekmarev & Stankus (1984).

The equivalence between the original jet problem modelled by a pulsed sonic source and the hypersonic source model is obtained by requiring that the hypersonic source and the choked source yield the same mass flux at a given distance x from the centre of symetry, i.e.

$$x_*^j \rho_* u_* = \Lambda^j \times 1 \times 1 = x^j \rho u. \tag{4.6}$$

The last equality explicitly shows that the mass flux at a given location in the steady expansion is the same for both sources. If we further assume that the source, and hence the entire flow field, is hypersonic (i.e. $M^2 \gg 1$), expression (4.4) evaluated in the hypersonic limit shows that the flow velocity is constant, given by

$$u = u_* = \left(\frac{\gamma_A + 1}{\gamma_A - 1} \right)^{1/2}. \tag{4.7}$$

Expressions (4.6) together with (4.7) provide the distribution of density and velocity with distance for the expansion from a hypersonic source.

The solution to the problem of a pulsed hypersonic radial source can be obtained using Chernyi's boundary-layer method obtained for strong shocks in the limit of γ approaching unity, also known as the Newtonian limit (Chernyi 1961). Since the maximal density behind an infinitely strong shock is given by $(\gamma + 1)/(\gamma - 1)$, the analysis takes the reciprocal of the maximal density as a small parameter

$$\varepsilon \equiv \frac{\gamma_A - 1}{\gamma_A + 1}, \tag{4.8}$$

which can be used to expand the position of a mass element x, its pressure and its density as

$$x = x^{(0)} + \varepsilon x^{(1)} + \cdots, \quad p = p^{(0)} + \varepsilon p^{(1)} + \cdots, \quad \rho = \frac{\rho^{(0)}}{\varepsilon} + \rho^{(1)} + \cdots. \tag{4.9}$$

The flow field can be separated in two parts. The first is the flow field between the interface (i) and the main shock (S_1). The second is the region between the secondary shock (S_2) and the interface (i). The flow between the source (denoted by an asterisk) and the secondary shock (S_2) is given by the steady expansion solution from a hypersonic source given by (4.6) and (4.7).

4.3. *Leading order of the hypersonic pulsed source problem*

At leading order, the position of a mass element shocked by either of the shocks S_1 or S_2 corresponds to the position of the shocks themselves, since the shocked layer of gas becomes infinitely dense and infinitely thin (see figure 13). Thus, at leading order, the radii of the secondary shock, contact surface and leading shock coincide:

$$x_i = x_{CS,0} \approx x_{S1,0} \approx x_{S2,0}. \tag{4.10}$$

The leading-order solution for the dynamics of the shocked gas interface (i.e. $x_i(t)$) can be formulated following the treatment of Chekmarev (1975). The conservation

of momentum (Chekmarev 1975) at time t for the gas layer bounded by the source $*$ and the leading shock S_1, yields

$$2\pi j x_*^j (\rho_* u_*^2 + p_*) = \frac{\mathrm{d}}{\mathrm{d}t} \left[(m_{Ai} + m_{Bi}) \frac{\mathrm{d}x_i}{\mathrm{d}t} + E_{*S_2} \right]. \tag{4.11}$$

The left-hand side is the momentum flux from the source. The first term on the right is the rate of change of the momentum of the mass bounded by the two shocks, where m_{Ai} and m_{Bi} denote the masses shocked by S_2 and S_1 respectively (see figure 13). The second term on the right is the rate of change of momentum of the gas in the free expansion bounded by the source and S_2.

Since the source is hypersonic (i.e. $M^2 \gg 1$), we have from the definition of Mach number that $p_* < \gamma p_* \ll \rho_* u_*^2$ and thus the static pressure can be neglected on the left-hand side of (4.11). Using (4.6), the term on the left of (4.11) can be re-written as $2\pi j u_* \Lambda^j$. The momentum E_{*S_2} is expressed as

$$E_{*S_2} = 2\pi j \int_{x_*}^{x_{S_2}} \rho u x^j \, \mathrm{d}x \approx 2\pi j (x_i - x_*) \Lambda^j \tag{4.12}$$

where use was made of (4.6) and (4.10). The mass m_{Bi} is the mass displaced by the interface i, i.e. the initial density multiplied by the volume of gas displaced by the interface:

$$m_{Bi} = \frac{\rho_{Bo}}{j+1} 2\pi j \left(x_i^{j+1} - x_*^{j+1} \right). \tag{4.13}$$

The mass m_{Ai} is the difference between the total mass escaping from the source in time t and the mass between the source and the shock S_2, yielding

$$m_{Ai} = 2\pi j \rho_* u_* x_*^j t - 2\pi j \int_{x_*}^{x_{S_2}} \rho x^j \, \mathrm{d}x \approx 2\pi j \Lambda^j (t - u_*^{-1}(x_i - x_*)) \tag{4.14}$$

where use was made of (4.6), (4.7) and (4.10). Expressions (4.12)–(4.14) can be substituted back in the momentum equation (4.11), which is integrated twice with the initial conditions

$$x_i(t=0) = x_*, \quad \frac{\mathrm{d}x_i}{\mathrm{d}t}(t=0) = u_* \tag{4.15}$$

yielding

$$\left(\frac{x_i}{x_*} - \frac{u_* t}{x_*} \right)^2 + \frac{2u_* \rho_{Bo} x_*^j}{\Lambda^j (j+1)(j+2)} \left(\frac{x_i}{x_*} \right)^{j+2} = 2 \left(\frac{x_i}{x_*} - \frac{u_* t}{x_*} \right) - \frac{2u_* \rho_{Bo} x_*^j}{\Lambda^j (j+1)} \left(\frac{x_i}{x_*} \right). \tag{4.16}$$

Since we are interested in the behaviour of the solution in the far field, where $(x_i/x_*) \gg 1$, we see that the terms on the right-hand side are of higher order than the terms on the left-hand side, and hence can be neglected. The resulting solution becomes independent of the radius of the hypersonic source, yielding

$$(x_i - u_* t)^2 + \frac{2u_* \rho_{Bo} x_i^{j+2}}{\Lambda^j (j+1)(j+2)} = 0. \tag{4.17}$$

The fact that the far-field solution becomes independent of the initial transients is the feature sought in the model, since different initial transients, such the shock tube solution in our original problem or the choked source in the one-dimensional idealization, are expected to give the same solution in the far field. Such behaviour is typical in explosion problems where different initial conditions yield the same leading-order solution in the far field. An example of such a dynamical behaviour is

the quasi-self-similarity of explosion phenomena from finite-dimension energy charges (Brode 1959). At scales much larger than the dimension of the initial charge, the flow field approaches the ideal self-similar strong blast wave solution of the point charge (Sedov 1959), provided the shock remains strong.

For convenience, following Chekmarev (1975), it is worth re-scaling the space and time coordinates according to

$$\xi \equiv \rho_{Bo}^{1/j} \frac{x}{\Lambda}, \quad \tau \equiv \rho_{Bo}^{1/j} \frac{t}{\Lambda}. \tag{4.18}$$

With these new variables, expression (4.17) can be solved for τ, yielding

$$\tau = u_*^{-1} \xi_i \pm \sqrt{\frac{2 u_*^{-1} \xi_i^{j+2}}{(j+1)(j+2)}} \tag{4.19}$$

where u_* is given by (4.7). The first term corresponds to the free expansion velocity, while the second corresponds to the effect of the gas ahead of the interface. The solution corresponding to the negative sign in front of the square root corresponds to an accelerating interface, which could perhaps be associated with an imploding shock, but can be ruled out for the present problem of an expanding shock supported by an expanding interface. The solution sought corresponds to the positive sign in front of the square root, which yields a decelerating interface. This completes the zeroth-order solution giving the dynamics of the jet head after the jet is started.

Note that a similar solution was postulated by Chekmarev & Stankus (1984) in an ad hoc fashion for sonic jets, yielding

$$\tau = \left(\frac{\gamma_A - 1}{\gamma_A + 1} \right) \xi_i + \sqrt{\frac{2 \Omega^{-(j+1)} \xi_i^{j+2}}{(j+1)(j+2)} \left(\frac{\gamma_A - 1}{\gamma_A + 1} \right)^{1/2}} \tag{4.20}$$

where the coefficient Ω takes on slightly sub-unity values (see below). The difference with the present model lies in the first term on the right-hand side of (4.20), governing the early dynamics of the jet. A comparison of our model and the one postulated by Chekmarev & Stankus with experimental data and our simulation results is given in §5.

4.4. *Higher-order solution: the shock and interface pressure evolution*

Once the motion of the interface, or piston, is known, the higher-order solution consists of determining the distribution of gas parameters between the interface and the shocks. In the following model, we will assume that both shocks S_1 and S_2 are strong, such that the interface solution derived above is expected to hold to higher orders. With this simplification, we can focus only on the flow field between the interface i and the shock S_1. We shall proceed as in Chernyi (1961) for the general derivation. It is useful to transform to a Lagrangian coordinate system, where we track the mass engulfed by the shock. A Lagrangian coordinate m written as

$$m = \int_0^x \rho x^j \, dx \tag{4.21}$$

corresponds to a quantity proportional to the amount of mass engulfed between the piston and the shock. The lower bound on the integral is taken as zero for simplicity, since we are now interested in the far-field solution given by (4.17), which eliminated the scale of the source at time zero. The conservation of mass, momentum and energy

for an inviscid gas are written as (Chernyi 1961)

$$\frac{\partial x}{\partial m} = \frac{1}{\rho x^j}, \quad \frac{\partial u}{\partial t} = \frac{\partial^2 x}{\partial t^2} = -x^j \frac{\partial p}{\partial m}, \quad \frac{\partial}{\partial t}\left(\frac{p}{\rho^\gamma}\right) = 0, \qquad (4.22)$$

where the partial derivative with time is taken while keeping m constant and denotes a material time derivative. Substituting (4.9) in (4.22) and using the Rankine–Hugoniot relations at the shock boundary, we can solve for the leading- and second-order solutions. We will omit the general derivation, which can be found in Chernyi (1961) for the general case, and instead focus on the particular case where the interface motion is given by a power law in time, and how it applies to the present problem.

By inspection of the evolution equation for $\xi_i(\tau)$ given by (4.19), we see that the first term on the right-hand side dominates at early times, while the second term, which has a larger power-law exponent than the first, dominates at later times. This suggests that the motion of the contact surface transits smoothly between two asymptotic limiting forms given by power-law solutions. Since the exponents of the power-law relationship do not differ significantly, we can approximate the dynamics as given by a local power-law solution approximated by

$$x_i = C\frac{t^{n+1}}{n+1} \qquad (4.23)$$

where n varies quasi-steadily as a function of t (or x_i). We have verified the validity of this quasi-steady assumption in the power-law exponent by comparing the results with the more general theory, which can be found in Chernyi (1961), and found an excellent agreement for the entire solution. From (4.17) and (4.18) and (4.23), the exponent n can be expressed in terms of the interface coordinate and its first two derivatives as

$$\frac{x_i(t)\ddot{x}_i(t)}{\dot{x}_i^2(t)} = \frac{\xi_i(\tau)\ddot{\xi}_i(\tau)}{\dot{\xi}_i^2(\tau)} = \frac{n}{n+1}, \qquad (4.24)$$

which permits us to determine the implicit weak dependence of $n(\tau)$ by evaluating the velocity and acceleration of the interface using (4.19), yielding

$$n(\tau) = -\left(\frac{j+2}{j} + \sqrt{\frac{8(j+1)}{j^2(j+2)u_*[\xi_i(\tau)]^j}}\right)^{-1}. \qquad (4.25)$$

Note that the implicit dependence $\xi_i(\tau)$ in (4.19) can be made explicit for both $j=1$, where it involves solving for the real roots of a third-degree polynomial, and for the much simpler case of $j=2$ where it involves seeking the roots of a second-degree polynomial. The variation of n given in (4.25) is shown graphically in figure 14 for $j=1,2$ and $\gamma=1.4$. Clearly, the value of n changes very slowly while τ varies by orders of magnitude, hence justifying the assumption of a quasi-steady exponent in the power-law approximation for the dynamics.

The quasi-steady assumption in the variation of n permits us to use directly the results derived by Chernyi for a piston propagating according to a power law in time and supporting a shock. A self-similar solution results in a power-law propagation of the shock with the same exponent. The ratio of the shock position and the interface position is also equal to the ratio of the speeds, which are both given by

$$\frac{x_{S1}}{x_i} = \frac{\dot{x}_{S1}}{\dot{x}_i} = \frac{\xi_{S1}}{\xi_i} = \frac{\dot{\xi}_{S1}}{\dot{\xi}_i} = \frac{1}{\Omega(\gamma_B, n, j)} \qquad (4.26)$$
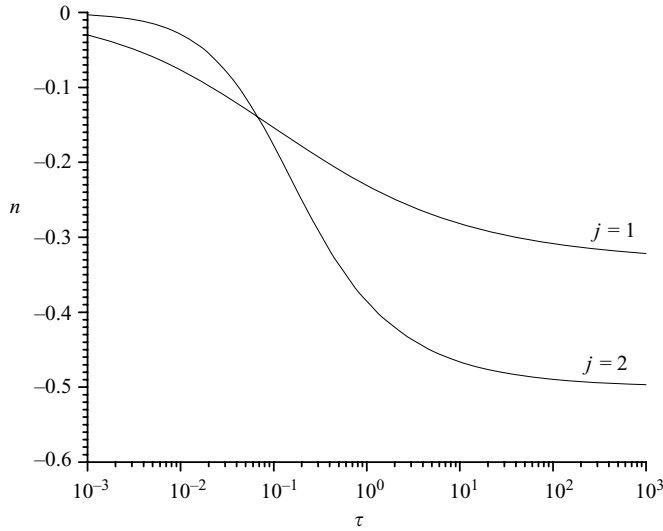
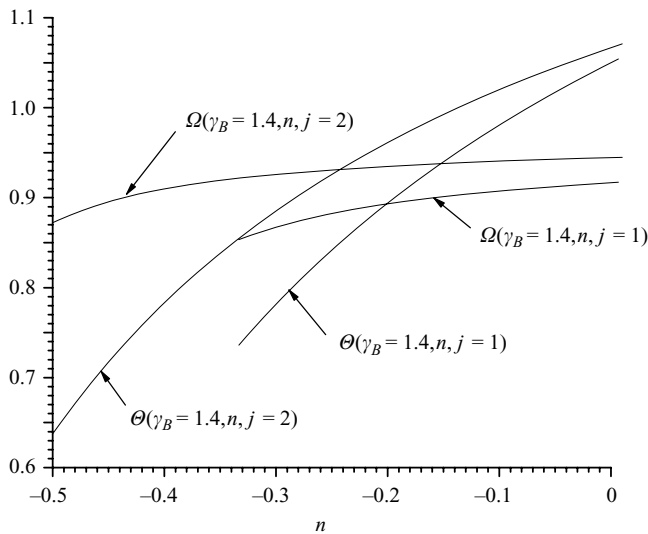FIGURE 14. The variation of exponent $n(\tau)$ for $\gamma = 1.4$ and $j = 1$ and 2.

FIGURE 15. Variation of functions Ω and Θ for $\gamma = 1.4$ and $j = 1$ and 2.

where the function $\Omega(\gamma_B, n, j)$ is given by

$$\Omega(\gamma_B, n, j) = 1 - \left(\frac{\gamma_B - 1}{\gamma_B + 1} \right) \frac{I(0, n, j)}{j + 1} \tag{4.27}$$

and is plotted in figure 15 for $j = 1, 2$ and $\gamma_B = 1.4$. The function I is defined as

$$I(\delta, n, j) \equiv \int_{\delta}^{1} s^{\frac{2n}{\gamma_B(j+1)(n+1)}} \left(1 + \frac{n(1 - s)}{(j + 1)(n + 1)} \right)^{-\gamma_B^{-1}} ds \tag{4.28}$$

and can be evaluated by numerical quadrature. With the shock velocity known, the shock pressure is obtained from the Rankine–Hugoniot relation across the strong

shock:

$$p_{S1}(t) = \frac{2}{\gamma_B + 1} \rho_{Bo} \dot{x}_{S1}^2(t) \tag{4.29}$$

or in terms of a similarity variable Ψ as

$$\Psi_{S1}(\tau) \equiv \frac{p_{S1}(\tau) a_{Bo}^2}{p_{Bo}} = \frac{2\gamma_B a_{Bo}^2 M_{s1}^2}{(\gamma_B + 1)} = \frac{2\gamma_B}{(\gamma_B + 1)} \left(\frac{\dot{\xi}_i(\tau)}{\Omega(\gamma_B, j, n(\tau))} \right)^2, \tag{4.30}$$

which defines in closed form the similarity law for the decay of shock pressure p_{S1} or for the shock Mach number in terms of the similarity time variable τ, the specific heat ratio γ_B, and the geometric index j.

Following Chernyi's derivation, the similarity law for the pressure evolution at the interface can also be expressed in closed form in terms of the shock pressure as

$$\frac{p_i}{p_{S1}} = \Theta(\gamma_B, n, j) \tag{4.31}$$

where the function $\Theta(\gamma_B, n, j)$ is given by

$$\Theta(\gamma_B, n, j) = \frac{\gamma_B + 1}{2} + \frac{n(\gamma_B + 1)}{2(j+1)(n+1)}$$
$$- \frac{\gamma_B - 1}{2} \frac{1}{j+1} \left(\frac{2n}{(j+1)(n+1)} + j + 2 \right) \int_0^1 I(s, n, j) \, \mathrm{d}s \tag{4.32}$$

and is plotted in figure 15 for $j = 1, 2$ and $\gamma_B = 1.4$.

Combining (4.30) and (4.31), the similarity law of the pressure evolution at the interface can be expressed as

$$\Psi_i(\tau) \equiv \frac{p_i(\tau) a_{Bo}^2}{p_{Bo}} = \frac{2\gamma_B \Theta}{(\gamma_B + 1)\Omega^2} \dot{\xi}_i^2(\tau). \tag{4.33}$$

An approximation to the pressure evolution at the interface is thus known analytically in closed form.

4.5. *The domain of validity of the solution*

As discussed in §3, the early time solution for the interface dynamics in the jet problem is given exactly by the one-dimensional shock tube solution. This solution remains valid until multi-dimensional expansions reach the axis, which occurs on a unity time scale. Only after some transient equilibration time for the multi-dimensional expansions, do we except the similarity solution derived above to be valid. The validity of the similarity solution is hence given approximately by

$$x, t \gg 1, \quad \text{i.e.} \quad \xi, \tau \gg \rho_{Bo}^{1/j}. \tag{4.34}$$

As the flow evolves, the solution's validity is expected to improve as long as the leading shock remains strong, such that the approximations made to obtain the shock and interface dynamics remain valid. The strong shock assumption requires that $(\dot{\xi}_{S1}/a_{Bo})^2 \approx (\dot{\xi}_i/a_{Bo})^2 \gg 1$. Expressing the interface velocity by differentiating (4.19), we obtain the following condition for the shock to remain strong and the model to remain valid:

$$\xi_i \ll \left(\frac{2}{j+2} (a_{Bo}^{-1} - u_*^{-1}) \sqrt{\frac{(j+1)(j+2)u_*}{2}} \right)^{2/j}. \tag{4.35}$$
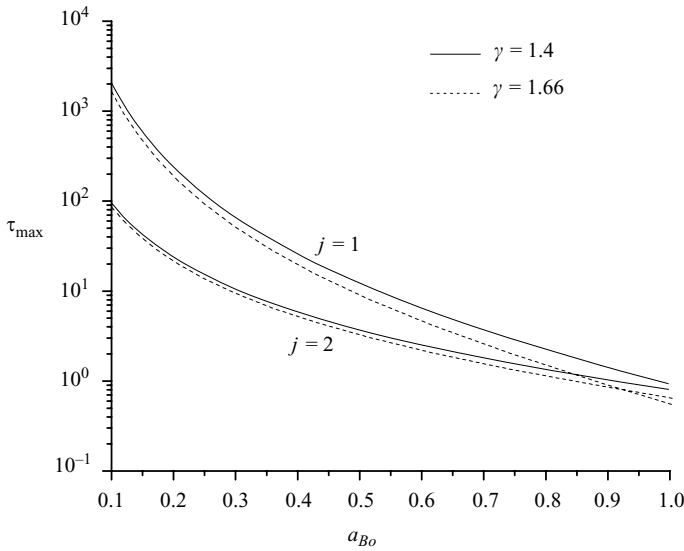
FIGURE 16. Upper bound time for the validity for the present model for slit and round jets.

The corresponding time τ_{max} can be obtained from (4.19), yielding the domain of validity of the solution

$$\rho_{Bo}^{1/j} \ll \tau \ll \tau_{max}. \tag{4.36}$$

Since the upper limit τ_{max} depends only on the non-dimensional sound speed a_{Bo}, it is worth representing this limit graphically for future reference, shown in figure 16 for $j = 1$ and $j = 2$ and $\gamma = 1.4$ and $\gamma = 1.66$.

The early time solution given by the one-dimensional shock tube problem can be incorporated when the pressure predicted in the similarity solution exceeds the shock tube solution. Defining a reference time $\tilde{\tau}$ when the pressure predicted by the similarity law is equal to the pressure given by the one-dimensional shock tube problem, the jet interface solution can be approximated well in a piecewise continuous fashion by

$$(p_i, \rho_{i_{A,B}}, T_{i_{A,B}}) = \begin{cases} (\tilde{p}_i, \tilde{\rho}_{i_{A,B}}, \tilde{T}_{i_{A,B}}), & \tau < \tilde{\tau} \\ (p_i(\tau), \rho_{i_{A,B}}(\tau), T(\tau)_{i_{A,B}}), & \tau \geqslant \tilde{\tau}. \end{cases} \tag{4.37}$$

Note that this does not introduce any fitting, as the similarity solution is in closed form. It only introduces a cutoff in the validity at early times, where the shock tube solution is assumed to be valid.

4.6. *The density and temperature at the contact discontinuity interface*

The self-similar model for the piston and shock motion predicts zero density (and infinite temperature) at the piston surface for a decelerating piston (Chernyi 1961), in spite of the finite pressure. This is a mathematical consequence of the self-similarity in piston-supported strong shocks, where the initial internal energy of the gas engulfed by the shock is neglected. This result can be shown from the exact self-similar solutions of strong shocks supported by pistons given by a power law, including the special case of an unsupported strong explosion (Sedov 1959). Similarly, for accelerating pistons, the density grows without bounds (and temperature vanishes) at the piston surface. Our jet problem illustrates both these effects near the gas interface separating the two gases. On the driven gas B side, the piston (i.e. the interface) decelerates the outward

motion of gas B and weakens the lead shock. Hence the density is expected to drop as the interface surface is approached. On the other hand, the interface accelerates the motion of gas A inward via the secondary shock, hence the reverse effect is expected of the density growing near the piston surface. One would hence expect that as the real jet evolves towards the asymptotic self-similar regime, a sharp density gradient is established at the gas interface of the same sign on each side of the interface. This is in good accord with the simulations (e.g. figures 9 and 12).

Since strict self-similarity poses a singularity in density and temperature at the piston surface, the real evolution of density and temperature at the interface can be obtained by relaxing the similarity hypothesis, and considering the real jet problem and the initial entropy gradients in the flow field given by the shock tube solution that prevails at early times. In the absence of any dissipative effect, this entropy difference remains in the flow at subsequent times. Furthermore, the numerical results also show that the jet head does not interact with any strong shocks and hence can be considered isentropic, at least until the end of the expansion region where the frontal interface is destabilized by the lateral vortex rings and associated shocklets (figure 10). Hence the evolution of the material layer near the contact surface during the dynamically similar regime of the jet is isentropic. Writing the conservation of entropy along a material trajectory, which corresponds to the gas interface, we obtain

$$\frac{\mathrm{D}s}{\mathrm{D}t} = \frac{\mathrm{D}}{\mathrm{D}t}\left(\frac{p}{\rho^{\gamma}}\right) = 0 \tag{4.38}$$

written here in the Eulerian fixed reference frame. We note that this relation is an exact statement of the conservation of entropy along a material surface, independent of the previous analysis and assumptions therein. Denoting the initial interface properties obtained from the solution of the one-dimensional shock tube problem by a tilda, the evolution of the density and temperature on each side of the contact surface are obtained by integrating (4.38) along the material path, yielding for a perfect gas

$$\rho_{iA}(\tau) = \tilde{\rho}_{iA}\left(\frac{p_i(\tau)}{\tilde{p}_i}\right)^{1/\gamma_A}, \qquad \rho_{iB}(\tau) = \tilde{\rho}_{iB}\left(\frac{p_i(\tau)}{\tilde{p}_i}\right)^{1/\gamma_B}. \tag{4.39}$$

$$T_{iA}(\tau) = \tilde{T}_{iA}\left(\frac{p_i(\tau)}{\tilde{p}_i}\right)^{(\gamma_A-1)/\gamma_A}, \qquad T_{iB}(\tau) = \tilde{T}_{iB}\left(\frac{p_i(\tau)}{\tilde{p}_i}\right)^{(\gamma_B-1)/\gamma_B}. \tag{4.40}$$

Since the pressure evolution $p_i(\tau)$ is known from the previous analysis to a good approximation, the density and temperature evolutions are thus known as a function of time with the same accuracy as the pressure evolution. This completes our solution for the evolution of the interface.

Note that the initial one-dimensional shock tube solution at the interface governs the subsequent density and temperature jump at the interface in the inviscid case. For example, taking the ratio of the two equations in (4.39) yields

$$\frac{\rho_{Ai}}{\rho_{Bi}}(\tau) = \frac{\tilde{\rho}_{Ai}}{\tilde{\rho}_{Bi}}\left(\frac{p_i(\tau)}{\tilde{p}_i}\right)^{(\gamma_B-\gamma_A)/\gamma_A\gamma_B} \tag{4.41}$$

which, if the isentropic indexes are equal, results simply in a constant density-jump discontinuity given by

$$\frac{\rho_{Ai}}{\rho_{Bi}} = \frac{\tilde{\rho}_{Ai}}{\tilde{\rho}_{Bi}} = \mathrm{const.} \tag{4.42}$$
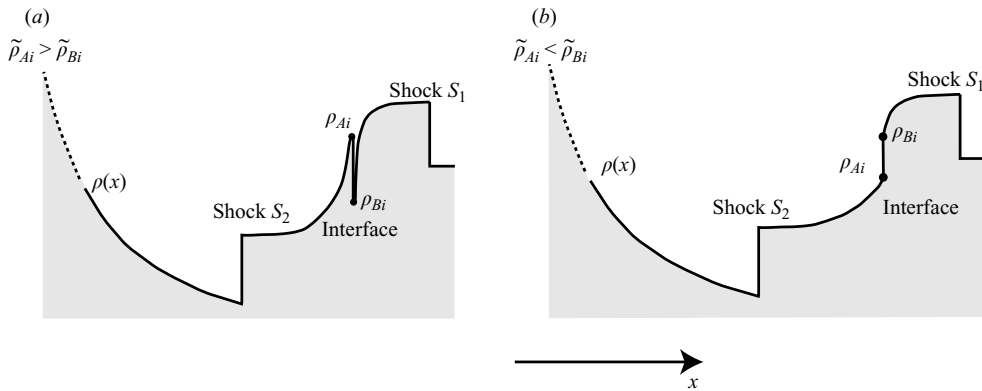
FIGURE 17. Density distributions for non-equal initial densities at the one-dimensional shock tube solution interface: (*a*) decelerating interface is unstable to Rayleigh–Taylor instability, (*b*) interface is stable.

Similar relations can also be written for the temperature ratio at the interface based on the original temperature ratio obtained from the one-dimensional shock tube problem. We thus see that in the absence of diffusion at the interface, the initial conditions of the jet problem completely determine the jumps in temperature and density at later times. Figure 17 illustrates qualitatively the resulting density profile for different initial density gradients at the contact surface. The numerical simulations verify this prediction, as can be seen from the profiles shown in figure 12, although some numerical diffusion is present making a quantitative comparison difficult.

4.7. *Rayleigh–Taylor instability*

Knowledge of the density evolution of the interface also permits us to evaluate the susceptibility of the interface to Rayleigh–Taylor instabilities (Taylor 1950). A decelerating interface devoid of any diffusive phenomena is unstable whenever $(\rho_{Ai}/\rho_{Bi}) > 1$. Expression (4.41) giving the density ratio at the interface in terms of the initial density ratio allows us to determine which initial conditions will give rise to the instability. For equal isentropic exponents γ in the two gases, (4.42) shows that the interface is always unstable for $(\tilde{\rho}_{Ai}/\tilde{\rho}_{Bi}) > 1$. For the hydrogen/air parameters used in the simulations above, neutral stability is obtained at equal densities at the interface corresponding to a rather high initial pressure ratio of 337 (see table 1). This is due to the low initial density of the compressed gas associated with its low molecular weight, in spite of it being compressed. However, heavier gases, or denser upstream stagnation states (as obtained in reflected shock tube experiments) may promote significant Rayleigh–Taylor instabilities during the jet establishment.

It is interesting to evaluate the conditions for which the growth rate of small-scale instabilities is comparable with the growth rate of the jet itself. Under these conditions, the instability may affect the development of the jet and compromise the model's validity. Alternatively, when the growth rate of the instability is smaller than that of the jet, initially small perturbations will apparently shrink when observed on the scale of the jet, and hence are expected to minimally influence the jet dynamics. If η denotes a perturbation of the position of the interface normal to its surface set initially to $\eta(t=0) = A\cos(ks)$, where s is a distance measured tangentially to the interface, we are seeking to express the growth rate of the ratio of the interface

perturbation and the interface location, i.e.

$$\frac{d \ln(\eta/x_i)}{dt} = \frac{d \ln \eta}{dt} - \frac{\dot{x}_i}{x_i}. \tag{4.43}$$

The first term on the right-hand side represents the growth of the perturbation due to the Rayleigh–Taylor instability, while the second represents the growth of the scale of the flow itself. Taylor's analysis (Taylor 1950) predicts a local growth rate of the perturbation given by

$$\frac{d \ln \eta}{dt} = \sqrt{-k\ddot{x}_i \frac{\rho_{Ai} - \rho_{Bi}}{\rho_{Ai} + \rho_{Bi}}} \tag{4.44}$$

where $\ddot{x}_i$ is the acceleration of the interface. The interface perturbation will grow at the same rate as the jet head when the right-hand side of (4.43) vanishes. The condition for an instability growth rate faster than that of the jet dimension is obtained from (4.44), (4.24) and (4.42) for gases with equal γ:

$$\frac{\tilde{\rho}_{Ai}}{\tilde{\rho}_{Bi}} \geqslant \frac{1 + \dfrac{1}{kx_i}\left(-\dfrac{n+1}{n}\right)}{1 - \dfrac{1}{kx_i}\left(-\dfrac{n+1}{n}\right)}. \tag{4.45}$$

The bracketed term is given from (4.24), with t evaluated at the corresponding x_i via (4.19). It is always greater than 1 for the range of permissible n. Expression (4.45) is always satisfied when the denominator is negative, giving explicitly the range of long-wavelength perturbations that will amplify faster than the jet growth in unstable jets:

$$k < \frac{1}{x_i}\left(-\frac{n+1}{n}\right). \tag{4.46}$$

Expressions (4.45) and (4.46) can be used to assess the jet surface stability during the jet release. The most critical point is the initial release, when x_i is small, and the bracket term is large, yielding short-wavelength amplification.

4.8. *Modelling the interface diffusion and jet ignition*

So far, we have assumed an inviscid diffusionless interface, i.e. a contact surface, governed by the Euler equations of motion. The implicit assumption was that of large Reynolds and Péclet numbers, such that diffusive effects are limited to a very narrow region of steep gradients present at such interfaces. Provided the boundary layer is much thinner than the scales of the flow, the boundaries of the thin boundary layer are only minimally affected by the diffusive fluxes and recover the solution derived above. We are interested in formulating the evolution of the boundary layer structure in the general case of a multi-component mixture involving diffusion and chemical reactions. The problem to be addressed is the diffusion of a cold fuel into a hot oxidizer, while the entire diffusion layer is subject to gasdynamic expansions. Ignition involving radical and thermal explosions may be achieved for sufficiently strong shocks and sufficiently low rates of expansion (Radulescu & Law 2005).

The natural framework of study is a one-dimensional Lagrangian formulation which follows the material interface and hence we can dispense with treating the convective fluxes in the description. Furthermore, since the scale of the boundary layer can be assumed much thinner than the embedding flow field, local curvature effects may be omitted, other than those due to global gasdynamic cooling. We use a

Lagrangian mass coordinate

$$\bar{m}' = \int_0^{\bar{x}} \bar{\rho} \, d\bar{x}. \tag{4.47}$$

The conservation of energy for a multi-component reacting fluid (Williams 1985) is given in dimensional form by

$$\bar{c}_p \frac{\partial \bar{T}}{\partial \bar{t}} = \frac{1}{\bar{\rho}} \frac{\partial \bar{p}}{\partial \bar{t}} + \frac{\partial}{\partial \bar{m}'} \left(\bar{\rho} \bar{\lambda} \frac{\partial \bar{T}}{\partial \bar{m}'} \right) - \sum_{k=1}^{K} \frac{\bar{h}_k \bar{w}_k}{\bar{\rho}} + \bar{\rho}^2 \frac{\partial \bar{T}}{\partial \bar{m}'} \sum_{k=1}^{K} \bar{c}_{p,k} \bar{D}_k \frac{\partial \bar{y}_k}{\partial m'} + \frac{\bar{\Phi}_{diss}}{\bar{\rho}} \tag{4.48}$$

where Dufour effects associated with thermal diffusion have been neglected. The consumption equation for the kth species also can be written as

$$\frac{\partial y_k}{\partial \bar{t}} = \frac{\partial}{\partial \bar{m}'} \left(\bar{\rho}^2 \bar{D}_k \frac{\partial \bar{T}}{\partial \bar{m}'} \right) + \frac{\bar{w}_k}{\bar{\rho}}. \tag{4.49}$$

In the above equations $\bar{c}_p$ is the mixture-averaged specific heat per unit mass, $\bar{\lambda}$ is the heat conduction coefficient, K the total number of species, $\bar{c}_{p,k}$ is the specific heat of the kth species, $\bar{h}_k$ is its enthalpy, $\bar{w}_k$ is its chemical production rate, $\bar{D}_k$ is its molecular diffusion coefficient, y_k its mass fraction and $\bar{\Phi}_{diss}$ is the viscous dissipation function. The last can be neglected since the flow in the vicinity of the interface in the frame of the interface is negligible (recall that the fluid velocity is matched in a one-dimensional gasdynamic contact surface). In words, expression (4.48) simply states that the rate of sensible enthalpy increase (decrease) following a fluid element is due to gasdynamic compression (expansion), heat conduction from neighbouring mass elements, chemical heat release and higher-order effects associated with non-equal specific heats of the different species and viscous dissipation of kinetic energy.

With the appropriate reaction rates and auxiliary relations for the mixture properties (see Williams 1985) and the ideal gas law for the kth species, the interface evolution is obtained by integrating (4.48) and (4.49), with initial conditions given by the one-dimensional shock tube problem across the interface for $(\bar{m}' < 0)$ in material A and $(\bar{m}' > 0))$ in material B. The sole influence of the gasdynamic evolution solved analytically above is through the prescription of the pressure time-derivative at the interface appearing in the first term on the right-hand side of (4.42), which can be expressed analytically from (4.37). This treatment is a valid approximation for assessing ignition associated with a radical explosion, since prior to ignition, the chemical processes release a small net amount of heat and do not affect the frozen flow field solved in the frozen jet problem above.

Since the expansion term acts as a heat sink through global expansion cooling, it can serve to quench the reaction process and prevent ignition, as already demonstrated in premixed systems (Lundstrom & Oppenheim 1969; Eckett, Quirk & Shepherd 2000). The analysis of the ignition process based on the numerical integration of (4.48) and (4.49), and formulation of ignition criteria based on simpler forms of (4.48) obtained under different approximations is currently under study.

5. Discussions

5.1. *Jet similarity*

The model formulated above for the evolution of the jet along its axis predicts that the jet dynamics are similar in terms of the space and time coordinates defined in terms of (4.18), with the sole parameters controlling the dynamics being the initial

non-dimensional density ρ_{Bo} and sound speed a_{Bo} of the receiver gas. These are listed in table 1 for the jet strengths studied. Using (2.10), these two parameters can be expressed in terms of useful dimensional quantities (which often serve as control parameters in experiments) as

$$\rho_{Bo} = \left(\frac{\bar{\rho}_{Bo}}{\bar{\rho}_{Ao}}\right)\left(\frac{\gamma_A + 1}{2}\right)^{1/(\gamma_A-1)} = \left(\frac{\bar{p}_{Bo}}{\bar{p}_{Ao}}\right)\left(\frac{\gamma_B}{\gamma_A}\right)\left(\frac{\bar{a}_{Ao}}{\bar{a}_{Bo}}\right)^2\left(\frac{\gamma_A + 1}{2}\right)^{1/(\gamma_A-1)}$$

$$= \left(\frac{\bar{p}_{Bo}}{\bar{p}_{Ao}}\right)\left(\frac{\bar{W}_B}{\bar{W}_A}\right)\left(\frac{\bar{T}_{Ao}}{\bar{T}_{Bo}}\right)\left(\frac{\gamma_A + 1}{2}\right)^{1/(\gamma_A-1)}, \tag{5.1}$$

$$a_{Bo}^2 = \left(\frac{\bar{a}_{Bo}}{\bar{a}_{Ac}}\right)^2 = \left(\frac{\bar{a}_{Bo}}{\bar{a}_{Ao}}\frac{\bar{a}_{Ao}}{\bar{a}_{Ac}}\right)^2 = \left(\frac{\bar{a}_{Bo}}{\bar{a}_{Ao}}\right)^2\left(\frac{\gamma_A + 1}{2}\right) = \frac{\gamma_B \bar{W}_A \bar{T}_{Bo}}{\gamma_A \bar{W}_B \bar{T}_{Ao}}\left(\frac{\gamma_A + 1}{2}\right). \tag{5.2}$$

Before investigating in detail the model predictions and the range of validity of the similarity relations predicted by the model, it is worth illustrating the scaling of the jets and the range of validity of the model graphically. Figure 18 shows the pressure and density fields obtained for the three jet strengths considered in the round-jet geometry at two fixed similarity times τ. The pressure and density are normalized by the scales associated with the reference receiver gas scales (recalling that $p_{Bo} = \gamma_{Bo}^{-1}\rho_{Bo}a_{Bo}^2$ and a_{Bo} is kept constant in the present simulations). At $\tau = 1.07$, we see that the weakest jet is still being formed, and the secondary inward shock has not yet formed. However, the second and third stronger jets have evolved over longer distances and now appear to be in very good mutual quantitative agreement. This illustrates well how the jet dynamics become similar once the jet is formed and the limitation of the model at early times when the jet is still under formation as discussed in §4.5.

The profiles taken at $\tau = 13.9$ shown in figure 18 illustrate the late jet formation stage characterized by the slender barrel/Mach shock structure and a complex strong acoustic radiation. These results were obtained at a lower resolution owing to the much larger computational domain (5 refinement levels with a minimum mesh spacing on the most resolved grid of 1/32). Although the local details of the unstable structure of the jets differ, their global morphology, pressure and density levels scale well according to the model predictions. We thus see that the jet dynamics scale according to the variables of the model.

The scaling of the jets may be best seen in the axial density profiles of figure 19 extracted from the profiles of figure 18 at the two values of τ. Clearly, the profiles are in very good agreement at both similarity time variables, with the exception of the weakest jet which is still under formation. Also shown in figure 19 is the steady expansion in the limit of hypersonic flow, i.e. given by (4.6), (4.7) and (4.18), which yields

$$\frac{\rho}{\rho_{Bo}} = u_*^{-1}\xi^{-j}, \tag{5.3}$$

which is in perfect agreement with the numerical results. This behaviour illustrates how the steady expansion wave from a sonic source becomes invariant under the new space coordinate ξ in the limit of hypersonic flow, i.e. once the flow has accelerated to hypersonic speeds. We thus see that the flow field becomes similar both in the shocked layers and in the steady expanding gases.

We may recall however that the scaling holds only in an asymptotic sense. Differences appear in the structure owing to the initial entropy differences at the contact surface, which are maintained in the limit of an isentropic flow along material trajectories. One example is the density gradient inversion for strong jets, such as the last jet shown in figures 18 and 19 for $p_{Ao}/p_{Bo} = 700$. The resulting effect is the
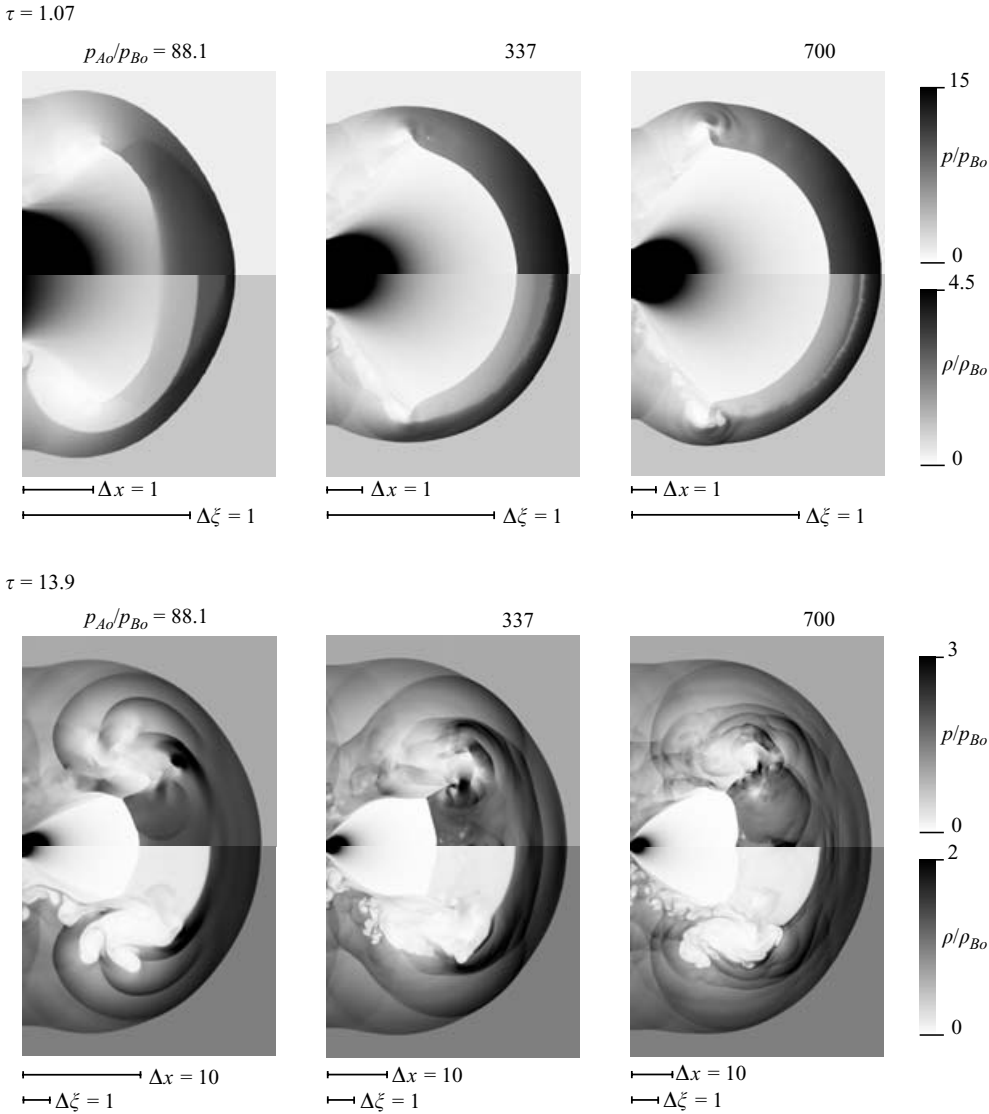
$\tau = 1.07$

FIGURE 18. Reduced pressure (upper half) and reduced density (lower half) fields in round jets of initial strengths $p_{Ao}/p_{Bo} = 88.1$, 337 and 700 taken at two similarity times $\tau = 1.07$ and $\tau = 13.9$ illustrating the approximate dynamic similarity of the flow field.

Rayleigh–Taylor (RT) instability which sets in along the material interface, as can be seen by inspection of the density contour shown in figure 18 for the stronger jet. We were however not able to fully study the RT instability owing to the lack of resolution at the contact surface and the ensuing numerical diffusion, which effectively broadens the interface and suppresses the instability at later times.

5.2. *The interface dynamics*

The evolution of the interface location computed for the three strengths of slit and round jets is shown in figure 20. The results consist of the highly resolved simulations at early times and the lower resolution results on wider domains obtained at later times, as described above. They are compared with the analytical prediction of the
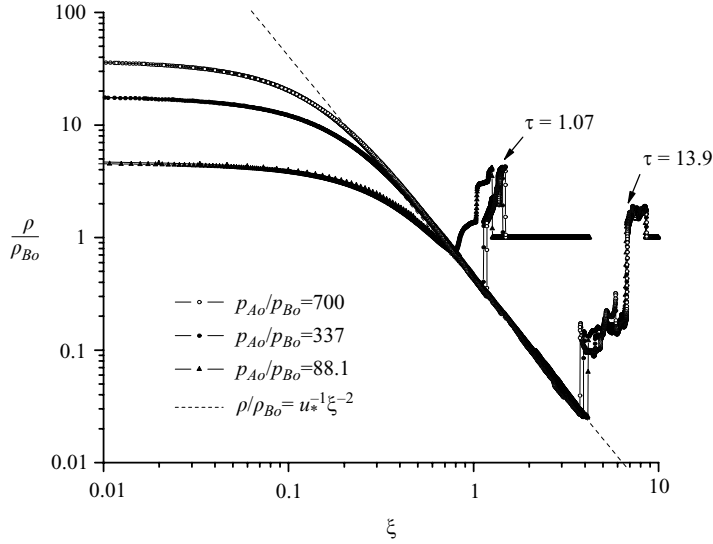
FIGURE 19. Reduced densities along the jet axis for the six jet conditions shown in figure 18; the dashed line denotes the steady expansion from a virtual hypersonic source in the similarity space variable.
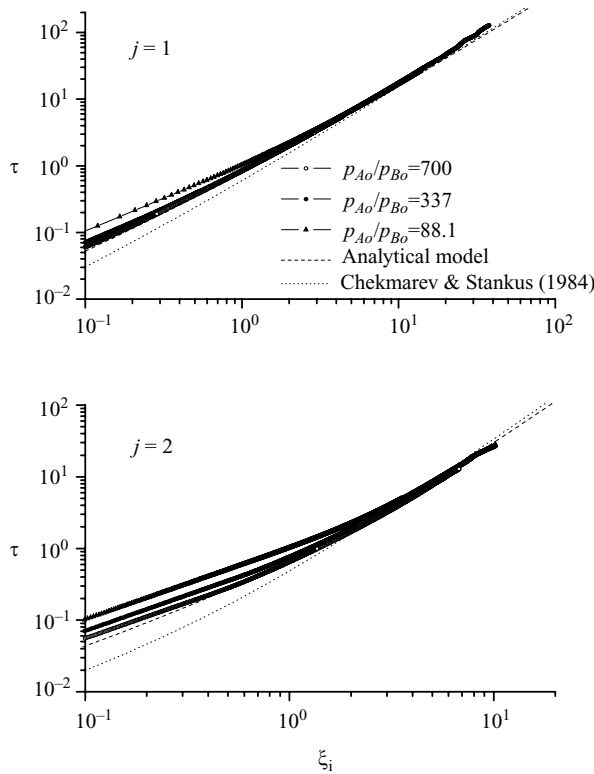

FIGURE 20. Evolution of the jet interface along its axis for slit jets ($j = 1$) and round jets ($j = 2$) obtained numerically for different strengths of the jet and comparison with the present analytical model and the model proposed by Chekmarev & Stankus (1984).
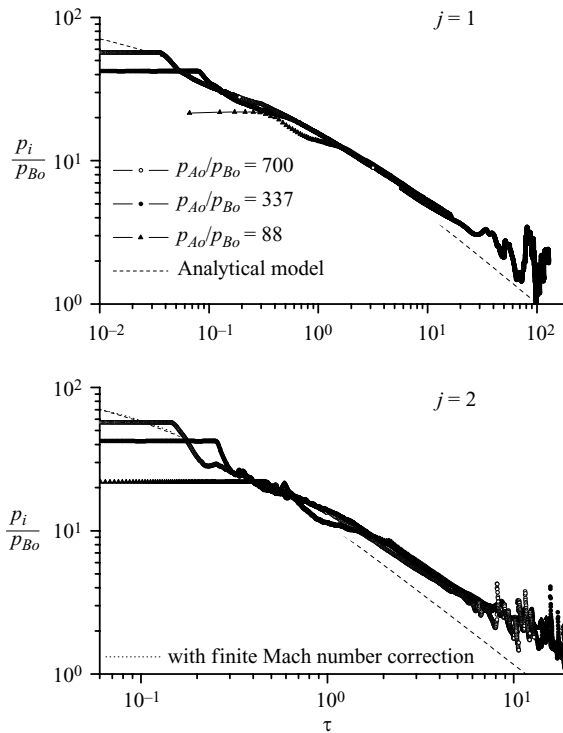
FIGURE 21. Evolution of the interface pressure along the jet axis for slit jets ($j = 1$) and round jets ($j = 2$) obtained numerically for different strengths of the jet and comparison with the present analytical model.

jet trajectory (equation (4.19)). Very good agreement with the model's prediction is observed after a critical time, corresponding approximately with the acoustic time $t \approx 1$. With increasing jet strength, the agreement occurs at earlier scaled times τ as indicated by the scaling of the jet similarity time variable in (4.18). The initial region of disagreement is the acoustic jet formation time. Some slight disagreement between the computational results and the prediction also occurs at the very late stages of the computation. This is when the shock can no longer be assumed to be strong, and the model becomes less accurate. For reference, also shown in figure 20 is the solution postulated by Chekmarev & Stankus (1984) (equation (4.20)). In the near field, their solution over-predicts the interface velocity by a factor of ~ 2.5, while good agreement is obtained with the present model in the far field, since they both have the same asymptotic form at late times.

5.3. *The pressure, density and temperature at the interface*

Figure 21 shows the evolution of the pressure at the jet interface along its axis for the different slit and round jets investigated. At early times, the pressure is constant, as given by the shock tube solution. After a few acoustic times of $t \sim 1$ (or $\tau \sim \rho_{Bo}^{1/j}$) the solutions become self-similar, as described above. The profiles are in good mutual agreement until later times when the jet pressure becomes comparable with the ambient pressure, the leading shock becomes weak and acoustic instabilities set-in. Interestingly, the acoustic instabilities also appear at approximately the same dynamical time in the different simulations. Also shown in figure 21 is the prediction

for the interface pressure obtained by the self-similar model based on strong shocks (equation (4.33)). The agreement is good for the entire range of the jet evolution, except during the initial transient when the one-dimensional shock tube solution is valid, and during the last stages of the jet evolution, when the lead shock becomes weak. The analytical prediction captures approximately the correct pressure even at the very beginning of the jet establishment. This unexpected agreement outside the range of validity of the model is a bonus feature of the model, which permits us to use the piecewise construction of the interface pressure proposed in (4.37) by artificially piecing together the shock tube solution with the dynamic parameter-free model.

At late times however, when the interface and shock pressure become weak, the present model under-predicts the interface pressure. This is the expected feature of the model, which is based on the strong shock assumption and neglects the contribution of the upstream internal energy of the gas. To illustrate the corrections that would occur by relaxing the strong shock assumption of the leading shock, while maintaining the same interface trajectory, we have computed the resulting pressure at the interface by the non-self-similar model of Chernyi (1961) by retaining supplementary terms involving the inverse square of the shock Mach number. The resulting prediction is shown in figure 21 for the round-jet geometry as a dotted line. As can be seen, the resulting prediction is identical to the strong shock prediction at early times, when the shock is strong. At intermediate times, it offers a more accurate prediction of the numerical results. At late times, however, it over-predicts the pressure at the interface. We thus see that the correction introduced by accounting for the strong shock effects in the pressure distribution, while maintaining the same interface trajectory as above, does not yield a uniformly valid correction until late times. This is apparently due to the fact that the interface trajectory itself should be corrected for the finite Mach number effects. Indeed, the resulting interface trajectory was obtained with the assumption that both the inward shock and lead shock are strong. At the later times, while the inward-facing shock approaches its strong shock limit, the outward-facing shock decays to a weak shock. This would correct the interface location to a smaller distance from the centre, hence a lower lead shock velocity and a lower pressure at the interface. A further discussion of these higher-order effects, which become important in weak jets or jets which have evolved to the weak limit, will be discussed below when comparing with experiments in weaker jets.

Once the interface pressure evolution is known, either from the numerical simulation or the analytic model, the density and temperature can be obtained via the isentropic relations in terms of the original gradients obtained from the shock tube solution, as outlined in §4.6. The accuracy of the density and temperature evolution at the interface is the same as that of the pressure prediction. As an example, the density and temperature profiles predicted via (4.39) and (4.40) are shown in figures 22 and 23 respectively for the slit jet with matched density. The results of the analytical prediction are found to capture very well their evolution at the interface. However, owing to numerical diffusion at the interface in the case of un-matched initial densities at the interface of the shock tube problem, we were not able to compare the numerical results with the inviscid predictions.

5.4. *Comparison with experiment*

We have further compared the model's predictions with experimental results for both slit jets and round jets. The results obtained by Belavin *et al.* (1973), reported in Chekmarev & Stankus (1984) with the present scalings, and those of Buckmaster (1964) for slit jets ($j = 1$) are shown in figure 24 for the range $0.3 < \tau < 20$. The slit
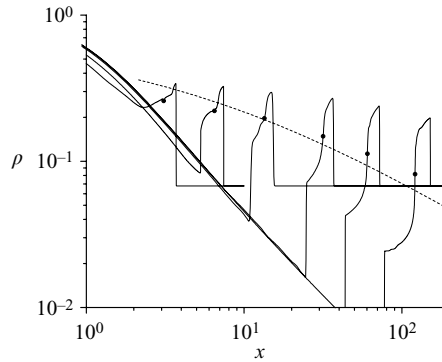
FIGURE 22. Interface density prediction (dashed line) and the density profiles obtained numerically for a slit jet with $p_{Ao}/p_{Bo} = 337$; circles denote the position of the interface between the two gases determined by tracking the passive scalar α.
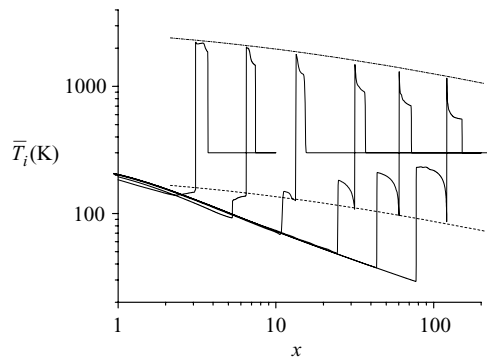

FIGURE 23. Interface temperature prediction: $\bar{T}_{Ai}$(dashed line) and $\bar{T}_{Bi}$ (dash-dot line) and calculated temperature profiles for the density-matched slit jet, i.e. $p_{Ao}/p_{Bo} = 337$, and $\bar{T}_{Ao} = \bar{T}_{Bo} = 300$ K.

jets were obtained in a shock tube set-up. A slit in the endwall of a shock tube permitted using the high pressure and temperature reflected-shock conditions as the stagnation state of the jet expansion. Buckmaster used incident shocks with a Mach number ranging between 6 and 8, yielding high acoustic speeds in the reflected-shock gases permitting the generation of strong jet-driven shocks. The corresponding non-dimensional sound speed in the receiver gas a_{Bo} was approximately 0.2. As discussed above, the non-dimensional sound speed a_{Bo} given by (5.2) controls the range of validity of the solution. From figure 16, we thus expect the present model to capture Buckmaster's experiments for $\tau \gg 300$. This condition is satisfied by the data. Reasonably good agreement is obtained with the present model. The experiments of Belavin *et al.* were also performed using the shock tube technique with an upstream stagnation temperature behind the reflected shock of 2500 K for the argon experiments and a 1700 K for the N_2 experiments, yielding values of a_{Bo} of approximately 0.4 and 0.5 respectively. From figure 16, we thus expect the model to capture the experimental data for $\tau \ll 20$, which is at the limit of the range of available data. The experimental results are in good agreement with the present model in the range of the model validity, although the shocks and interfaces propagate at slightly higher velocities
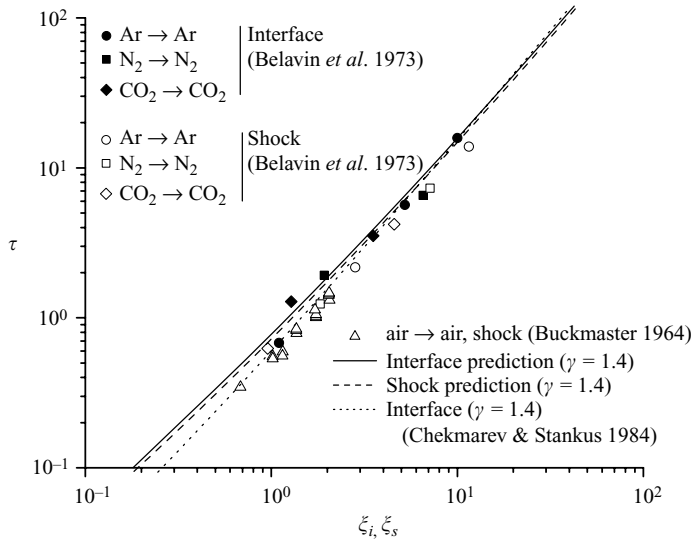
FIGURE 24. Comparison of the predicted shock and interface locations for strong slit jets ($j = 1$) with experimental data in different gases.
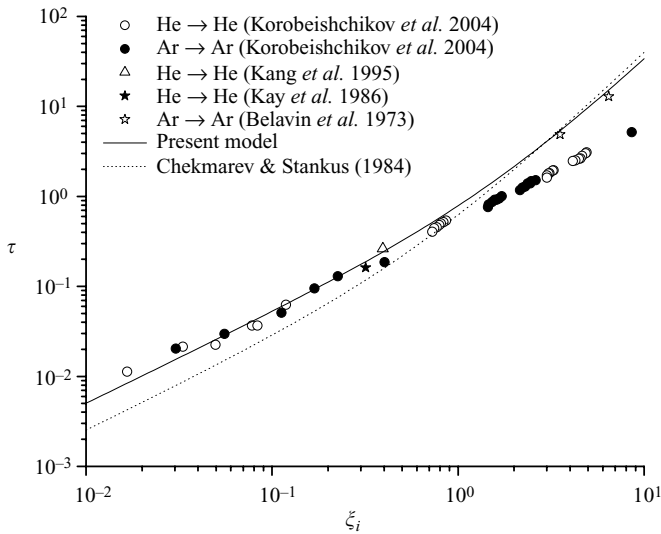

FIGURE 25. Comparison of the predicted interface location for strong round jets ($j = 2$) with experimental data in monatomic gases.

than predicted. Note also that over the limited range of experimental data obtained for slit jets, the model of Chekmarev & Stankus (1984) yields the same accuracy.

Round jets are in general more easily implemented experimentally and significantly more data are available in the literature, although the data are quite scarce for the strong jet conditions of interest here. Here we compare our model's predictions in figures 25 and 26 with the measured interface trajectory by Belavin *et al.* (1973) (reported in non-dimensional form by Chekmarev & Stankus 1984), Korobeishchikov *et al.* (2004), Kang *et al.* (1995) and Kay, Raymond & Rice (1986) for various gas combinations. The experiments of Belavin *et al.* were performed under the same conditions as described above for slit jets. From Figure 16, we thus expect the
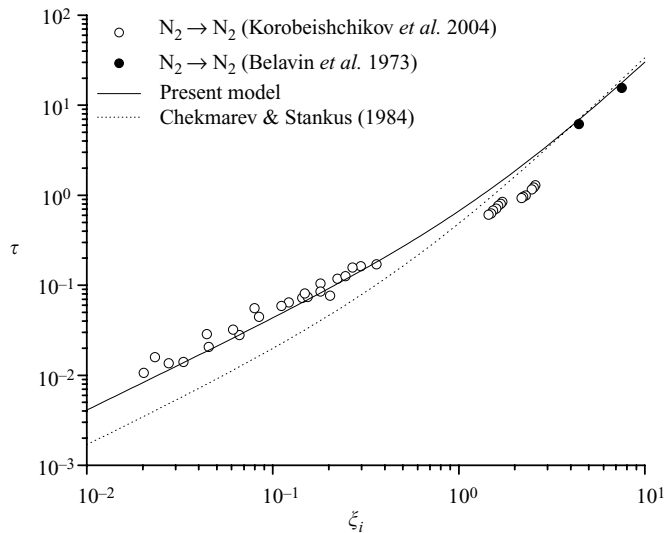
FIGURE 26. Comparison of the predicted interface location for strong round jets ($j = 2$) with experimental data of N_2 jets.

model to capture the experimental data for $\tau \ll 5$. Although the experimental data lie outside this range, a perhaps fortuitous good agreement is obtained. The data of Korobeishchikov *et al.*, of Kang *et al.* and of Kay *et al.* were obtained with matched initial stagnation temperatures, yielding values of $a_{Bo} \approx 1$. From figure 16, the validity of the model would be for conditions such that $\tau \ll 1$. By inspection of the data in figures 25 and 26, we see that excellent agreement is obtained with the model in the predicted range, while the model of Chekmarev & Stankus (1984) fails to capture the early evolution. Outside the range of validity of the model, when the leading shock becomes weak, the model fails to capture the experimental data, with interfaces propagating much faster than predicted.

The conclusion that can be drawn from the comparison with available experimental data for both slit and round jets is that over the range of validity of the model, the agreement is from good to excellent. Nevertheless, for weaker jets the model fails to capture the experimental results. Note that at these stages a much more complex situation arises in the experiments than captured in the model. Not only would finite Mach number corrections be necessary to account for the dynamics of the jet, as discussed above in the framework of the developed model, but the jet itself is expected to be highly unstable, as observed both in the present calculations and experimentally (e.g. Golub 1994). Further work is required to elucidate the jet scaling at these later times.

6. Conclusions and prospects

In the present study, we have studied the hydrodynamic evolution of highly under-expanded jets and formulated an approximate similarity solution for the jet evolution in the limit of negligible transport phenomena. The results were found to be in very good agreement with numerical simulations and available experiments over the range of validity of the model. The model can be used to study local diffusive and reactive phenomena operating on the scales of the interface by using the analytic solutions derived in the inviscid case as boundary conditions in the diffusive layer. Although

the model is limited to quasi-one-dimensional phenomena occurring at the frontal jet interface while the jet is still strong, it can be used to determine the conditions for the jet self-ignition exactly in the hottest region of the flow, which experiences the slowest volumetric expansion and is the first ignition locus (Golub *et al.* 2005; Liu *et al.* 2005).

The present numerical simulations also indicated that the jet becomes acoustically unstable and starts radiating shocks when it becomes weak. The frontal interface is thus susceptible to both Rayleigh–Taylor and shock–density layer instabilities, which can enhance turbulent mixing. These instabilities are particularly important in the reactive jet case, since they can enhance the ignition process of the entire jet and lead to the establishment of turbulent jet flames. These phenomena are not accounted by the present model and require future study.

REFERENCES

AMANN, H. O. 1969 Experimental study of the starting process in a reflection nozzle. *Phys. Fluids* **12** Supp. I, I150–I153.

ASHKENSAS, H. & SHERMAN, F. S. 1964 The structure and utilization of supersonic free jets in low density wind tunnels. In *Proc. 4th Intl Symp. on Rarefied Gas Dynamics, University of Toronto*, Vol. 2 (ed. J. H. Leeuw). Academic.

BELAVIN, A. V., GOLUB, V. V., NABOKO, I. M. & OPARA, A. M. 1973 Study of the structure of a time-dependent flow created by an emerging stream of shock-heated gas. *J. Appl. Mech. Tech. Phys.* **5**, 34–40.

BOCHKAREV, A. A., REBROV, A. K. & CHEKMAREV, S. F. 1969 Hypersonic spherical expansion of a gas with stationary shock wave. *J. Appl. Mech. Tech. Phys.* **10**, 62–67.

BOYER, D. W. 1960 An experimental study of the explosion generated by a pressurized sphere. *J Fluid Mech.* **9**, 401–429.

BRODE, H. L. 1959 Blast wave from a spherical charge. *Phys. Fluids* **2**, 217–229.

BUCKMASTER, J. D. 1964 An investigation of cylindrical starting flows. *AIAA J.* **2**, 1649–1650.

CAMPARGUE, R. 1984 Progress in overexpanded supersonic jets and skimmed molecular-beams in free-jet zones of silence. *J. Phys. Chem.* **88**, 4466–4474.

CHAINEAUX, J., MAVROTHALASSITIS, G. & PINEAU, J. 1991 Modelization and validation tests of the discharge in air of a vessel pressurized by a flammable gas. In *Dynamics of Detonations and Explosions: Explosion Phenomena* (ed. A. L. Kuhl, J.-C. Leyer, A. A. Borisov & W. A. Sirignano) Progress in Astronautics and Aeronautics, Vol. 134, pp. 104–137, AIAA.

CHEKMAREV, S. F. 1975 Nonsteady radial expansion of a gas into a flooded space from a suddenly turned on steady source. *J. Appl. Mech. Tech. Phys.* **2**, 209–216.

CHEKMAREV, S. F. & STANKUS, N. V. 1984 Gasdynamic model and similarity relations for the starting process in supersonic nozzles and jets. *Sov. Phys. Tech. Phys.* **29**, 920–925.

CHERNYI, G. G. 1961 *Introduction to Hypersonic Flow*. Academic.

DRYER, F. L., CHAOS, M., ZHAO, Z., STEIN, J. N. & ALPERT, J. Y. & HOMER, C. J. 2007 Unique ignition potentials for pressurized releases of hydrogen and natural gas into air. *Combust. Sci. Tech.* **179**, 1–32.

ECKETT C. A., QUIRK, J. J. & SHEPHERD, J. E. 2000 The role of unsteadiness in direct initiation of gaseous detonations. *J. Fluid Mech.* **421**, 147–183.

FALLE, S. A. E. G. 1991 Self-similar jets. *Mon. Not. R. Astron. Soc.* **250**, 581–596.

FALLE, S. A. E. G. & GIDDINGS, J. R. 1993 Body capturing. In *Numerical Methods for Fluid Dynamics* (ed. K. W. Morton & M. J. Baines), vol. 4, pp. 337–343. Clarendon.

FALLE, S. A. E. G. & KOMISSAROV, S. S. 1996 An upwind scheme for relativistic hydrodynamics with a general equation of state. *Mon. Not. R. Astron. Soc.* **278**, 586–602.

FRIEDMAN, M. P. 1961 A simplified analysis of spherical or cylindrical blast waves. *J. Fluid Mech.* **11**, 1–15.

GOLUB, V. V. 1994 Development of shock wave and vortex structures in unsteady jets. *Shock Waves* **3**, 279–285.

GOLUB, V. V., BAZHENOVA, T. V., BRAGIN, M. V., IVANOV, M. F., SCHERBAK, S. B. & VOLODIN, V. V. 2005 Self-ignition of pulse sonic hydrogen jet. In *Nonequilibrium processes* (ed. G. Roy, S. Frolov & A. Starik), vol. 1, pp. 44–45. Torus Press.

GROETHE, M., MERILO, E., COLTON, J., CHIBA, S., SATO, Y. & IWABUCHI, H. 2005 Large-scale hydrogen deflagrations and detonations. *Intl Conference on Hydrogen Safety, Pisa, Italy, September 8–10*.

HURLE, I. R. & HERTZBERG, A. 1965 Electronic population inversions by fluid-mechanical techniques. *Phys. Fluids* **8**, 1601–1607.

ISHII, R., FUJIMOTO, H., HATTA, N. & UMEDA, Y. 1999 Experimental and numerical analysis of circular pulse jets. *J. Fluid Mech.* **392**, 129–153.

KANG, W. K., KIM, E. J., CHOI, C. J., JUNG, K. W. & JUNG, K. H. 1995 Time-resolved molecular-beam characteristic in a pulsed supersonic jet. *Bull. Korean Chem. Soc.* **16**, 238–243.

KAY, B. D., RAYMOND, T. D. & RICE, J. K. 1986 Time-of-flight characterization of pulsed supersonic helium free-jet expansions. *Rev. Sci. Instrum.* **57**, 2266–2273.

KOROBEISHCHIKOV, N. G., ZARVIN, A. E. & MADIRBAEV, V. ZH. 2004 Hydrodynamics of pulsed supersonic underexpanded jets: spatiotemporal characteristics. *Tech. Phys.* **49**, 973–981.

LACERDA, N. L. 1986 On the start up of supersonic underexpanded jets. PhD Thesis, California Institute of Technology, Pasadena, California.

LIEPMANN, H. W. & ROSHKO, A. 2001 *Elements of Gasdynamics*. Dover.

LIU Y.-F., TSUBOI, N., SATO, H., HIGASHINO, F. & HAYASHI, A. K. 2005 Direct numerical simulation on hydrogen fuel jetting from high pressure tank. *20th Intl Colloquium on the Dynamics of Explosions and Reactive Systems, McGill University, Montreal, Canada, July 31–August 5 2005*, paper 122 (on CD-Rom).

LUNDSTROM, E. A. & OPPENHEIM, A. K. 1969 On the influence of non-steadiness on the thickness of the detonation wave. *Proc. R. Soc. Lond.* A **310**, 463–478.

MATÉ, B., GRAUR, I. A., ELIZAROVA, T., CHIROKOV, I., TEJEDA, G., FERNANDEZ, J. M. & MONTERO, S. 2001 Experimental and numerical investigation of an axisymmetric supersonic jet. *J. Fluid Mech.* **426**, 177–197.

MILLER, D. R. 1988 Free jet sources. In *Atomic and Molecular Beam Methods* (ed. G. Scoles), Vol. I, pp. 14–53. Oxford University Press.

NOBOKO, I. M., BAZHENOVA, T. V., OPARA, A. I. & BELAVIN, V. A. 1972 Formation of a jet of shock-heated gas outflowing into evacuated space. *Astronaut. Acta* **17**, 653–658.

NABOKO, I. M., GOLUB, V. V., EREMIN, A. V., KOCHNEV, V. A. & KULIKOVSKI, A. A. 1977 Wave structure and density distribution in a non-stationary gas jet. *Arch. Mech.* **29**, 69–80.

NABOKO, I. M., KUDRYAVTSEV, E. M., OPARA, A. I. & GOLUB, V. V. 1974 Structure of a shock heated gas flow under pulsed gas-dynamic laser conditions. *High Temp.* **12**, 105–109.

QUIRK, J. J. 1992 A contribution to the great Riemann solver debate. *ICASE Rep.* 92–64.

RADULESCU, M. I. & LAW, C. K. 2005 Development and ignition of a strong under-expanded jet. *Bull. Am. Phys. Soc.* **50**, No. 9.

SEDOV, L. I. 1959 *Similarity and Dimensional Methods in Mechanics*. Academic.

SHARPE, G. J. 2001 Transverse waves in numerical simulations of cellular detonations. *J. Fluid Mech.* **447**, 31–51.

SKEWS, B. W. 1967 Shape of a diffracting shock wave. *J. Fluid Mech.* **29**, 297–304.

SMITH, C. E. 1966 The starting process in a hypersonic nozzle. *J. Fluid Mech.* **24**, 625–640.

TAYLOR, G. 1950 The instability of liquid surfaces when accelerated in a direction perpendicular to their planes. I. *Proc. R. Soc. Lond.* A **201**, 192–196.

WILLIAMS, F. A. 1985 *Combustion Theory*. Perseus Books.

WOLANSKI, P. & WOJCICKI, S. 1973 Investigation into the mechanism of the diffusion ignition of a combustible gas flowing into an oxidizing atmosphere. *Proc. Combust. Inst.* **14**, 1217–1224.